



**HAL**  
open science

## New cosmogenic nuclide constraints on Late Glacial and Holocene glacier fluctuations in the sub-Antarctic Indian Ocean (Kerguelen Islands, 49°S)

Joanna Charton, Irene Schimmelpfennig, Vincent Jomelli, Regis Braucher, Guillaume Delpech, Pierre-Henri Blard, Deborah Verfaillie, Vincent Favier, V.R. Rinterknecht, Hugues Goosse, et al.

### ► To cite this version:

Joanna Charton, Irene Schimmelpfennig, Vincent Jomelli, Regis Braucher, Guillaume Delpech, et al.. New cosmogenic nuclide constraints on Late Glacial and Holocene glacier fluctuations in the sub-Antarctic Indian Ocean (Kerguelen Islands, 49°S). *Quaternary Science Reviews*, 2022, 283, pp.107461. 10.1016/j.quascirev.2022.107461 . hal-03625148

**HAL Id: hal-03625148**

**<https://hal.science/hal-03625148>**

Submitted on 30 Mar 2022

**HAL** is a multi-disciplinary open access archive for the deposit and dissemination of scientific research documents, whether they are published or not. The documents may come from teaching and research institutions in France or abroad, or from public or private research centers.

L'archive ouverte pluridisciplinaire **HAL**, est destinée au dépôt et à la diffusion de documents scientifiques de niveau recherche, publiés ou non, émanant des établissements d'enseignement et de recherche français ou étrangers, des laboratoires publics ou privés.

1 **New cosmogenic nuclide constraints on Late Glacial and Holocene glacier fluctuations**  
2 **in the sub-Antarctic Indian Ocean (Kerguelen Islands, 49°S)**

3

4 Joanna Charton<sup>a</sup>, Irene Schimmelpfennig<sup>a</sup>, Vincent Jomelli<sup>a</sup>, Guillaume Delpech<sup>b</sup>, Pierre-  
5 Henri Blard<sup>c</sup>, Régis Braucher<sup>a</sup>, Deborah Verfaillie<sup>a,d</sup>, Vincent Favier<sup>e</sup>, Vincent Rinterknecht<sup>a</sup>,  
6 Hugues Goosse<sup>d</sup>, Xavier Crosta<sup>f</sup>, Léo Chassiot<sup>g</sup>, Léo Martin<sup>h</sup>, Damien Guillaume<sup>i</sup>, Claude  
7 Legentil<sup>j</sup>, ASTER Team<sup>a,1</sup>

8

9 <sup>a</sup>*Aix Marseille Univ, CNRS, IRD, INRAE, CEREGE, Aix-en-Provence, France*

10 <sup>b</sup>*Université Paris-Saclay, CNRS, GEOPS - France*

11 <sup>c</sup>*Université de Lorraine, CNRS, CRPG - France*

12 <sup>d</sup>*Earth and Life Institute, Université catholique de Louvain, Louvain-la-Neuve, Belgium*

13 <sup>e</sup>*Institut des Géosciences de l'Environnement, Université Grenoble Alpes, CNRS, Grenoble,*  
14 *France*

15 <sup>f</sup>*UMR CNRS 5805 EPOC, Université de Bordeaux, France*

16 <sup>g</sup>*Université Laval, Département de Géographie, Québec, Canada*

17 <sup>h</sup>*Faculty of Geosciences, Utrecht University, Utrecht, The Netherlands*

18 <sup>i</sup>*Univ Lyon, UJM-Saint-Etienne, UCBL, ENSL, CNRS, LGL-TPE UMR5276 – France*

19 <sup>j</sup>*Université Paris 1 Panthéon-Sorbonne, CNRS Laboratoire de Géographie Physique -*  
20 *France*

21

22 <sup>1</sup>*ASTER Team: Georges Aumaître, Didier Bourlès ( † ), Karim Keddadouche*

23 \*Corresponding author: Joanna Charton, [charton@cerege.fr](mailto:charton@cerege.fr)

24

25

26 Abstract:

27 Cosmogenic nuclide dating of glacial landforms on the Kerguelen Archipelago (49°S, 69°E)  
28 gives the opportunity to study multi-millennial glacier fluctuations within the sub-Antarctic  
29 sector of the Indian Ocean. We here dated such geomorphic features to provide time  
30 constraints over the last 17,000 years using *in situ*-produced  $^{36}\text{Cl}$  in three glacial valleys: Val  
31 Travers valley, Ampere Glacier valley and Arago Glacier valley. For the first time, a  
32 combination of *in situ*-produced  $^{36}\text{Cl}$  and  $^{10}\text{Be}$  dating and  $^{26}\text{Al}/^{10}\text{Be}$  ratios analysis was  
33 performed in the quartz-bearing syenite boulders of the Arago Glacier site. In addition, a  
34 Bayesian approach was computed to obtain a better constraint on moraine dating. Glacial  
35 advances occurred during the Late Glacial at  $16.0 \pm 1.9$  ka and at  $12.9 \pm 1.7$  ka in Val  
36 Travers, and at  $13.6 \pm 1.8$  ka in Arago Glacier valley, probably linked to the Heinrich Stadial  
37 1 and/or Antarctic Cold Reversal events, respectively. This suggests that all glaciers at this  
38 latitude were broadly sensitive to the large-scale climatic signal of the Antarctic Cold  
39 Reversal. So far, no Early nor Mid-Holocene moraines have been found in the glacial valleys  
40 on Kerguelen, indicating that the glaciers had probably receded significantly during these  
41 periods. This is in agreement with previously determined  $^{14}\text{C}$  ages from peat bogs, which  
42 suggest extensive deglaciation during several millennia of the Holocene period. Samples  
43 from glacially-polished bedrock surfaces (ranging from  $\approx 4.4$  ka to  $\approx 14$  ka) at Ampere  
44 Glacier site also suggest that this valley was ice free for several millennia during the  
45 Holocene. Finally, glaciers seem to have re-advanced only during the Late Holocene,  
46 especially within the last millennium, at  $\approx 1$  ka,  $\approx 430$  yr and  $\approx 300$  yr. A comparison of this  
47 new dataset with the available  $^{10}\text{Be}$  ages from other southern mid-latitude regions during the  
48 Holocene allows the identification of three different glacier evolution patterns. We suspect

49 that variations of Kerguelen glaciers, which are located in the Southern Indian Ocean, were  
50 controlled by the combined effects of sea surface temperature related to the variations of the  
51 Antarctic Polar Front and fluctuations of precipitation related to long-term variations of the  
52 Southern Annular Mode.

53 Keywords: glacier fluctuations, paleoclimate, <sup>36</sup>Cl CRE dating, <sup>10</sup>Be CRE dating, Late  
54 Glacial, Antarctic Cold Reversal, Holocene, southern mid-latitudes, sub-Antarctic, Kerguelen  
55 Islands.

56

57

58

59

60

61

62

63

64

65

66

67

68

69

70

71

72

## 73 1. Introduction

74

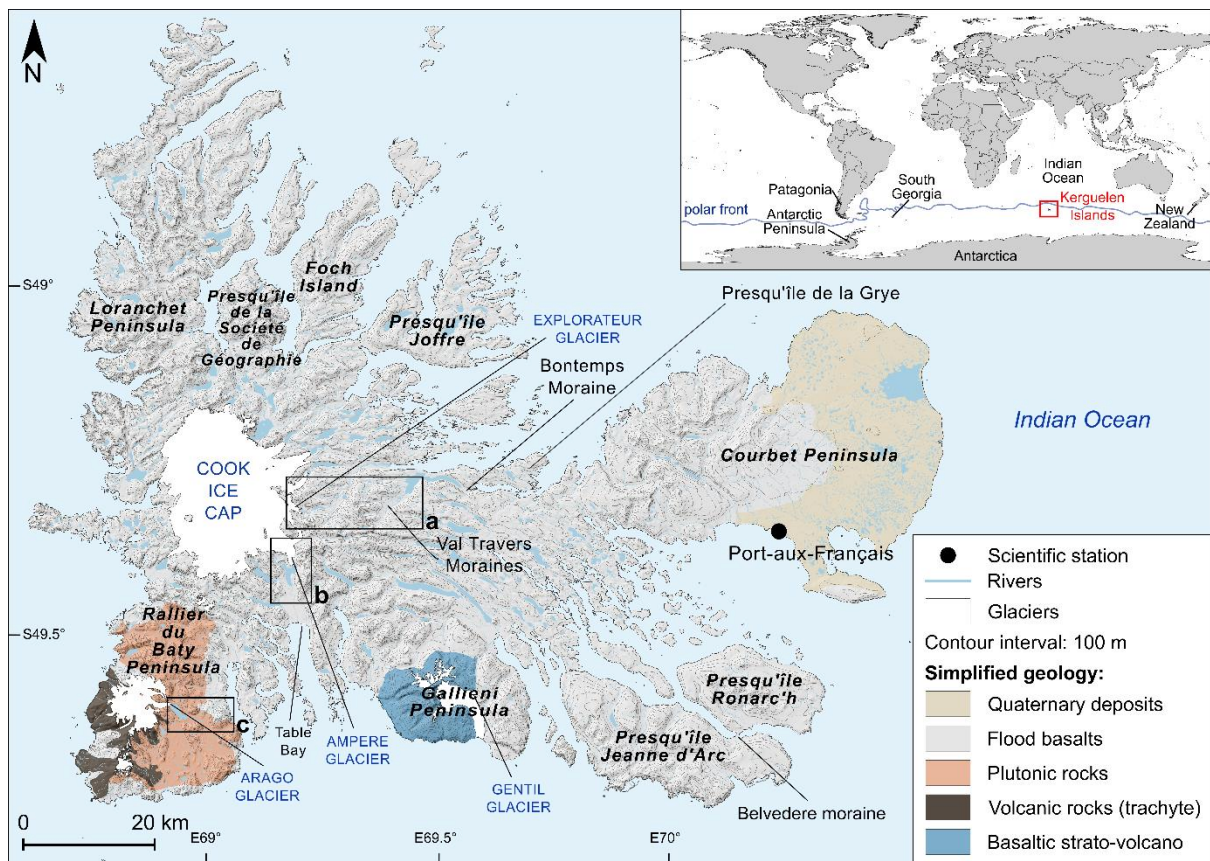
75 Reconstruction of the long-term evolution of glacier fluctuations provides the opportunity to  
76 better understand their sensitivity to multi-millennial and -centennial climate change, in  
77 particular to the variability of air temperature and precipitation. Cosmic ray exposure (CRE)  
78 dating of glacio-geomorphologic formations, such as moraines, erratic boulders and glacially-  
79 eroded bedrock, using *in situ*-produced cosmogenic nuclides is particularly suited to  
80 reconstruct past glacier chronologies (Balco et al., 2020). Most paleoglacier records in the  
81 mid-latitudes of the Southern Hemisphere are based on the well-constrained *in situ*  $^{10}\text{Be}$   
82 dating method applied to quartz-bearing moraine boulders (*e.g.* Putnam et al., 2012;  
83 Reynhout et al., 2019). In only few studies moraine chronologies are established from the less  
84 commonly used *in situ*  $^{36}\text{Cl}$  and  $^3\text{He}$  (Eaves et al., 2019; Rudolph et al., 2020). A consistent  
85 glacier evolution has been evidenced in various regions of the mid-latitudes of the Southern  
86 Hemisphere during the Holocene (11.7 ka - present) with glaciers located in New Zealand  
87 (*e.g.* Putnam et al., 2012), South Georgia (*e.g.* Bakke et al. 2021) and Patagonia (*e.g.*  
88 Reynhout et al., 2019) experiencing their maximal Holocene extent during the Early  
89 Holocene (11.6 – 8 ka), followed by a gradual decrease of glacier extent throughout time.  
90 This multi-millennial trend is attributed to the variation in summer insolation (Putnam et al.,  
91 2012) and at an intra-millennial scale to variations in precipitation intensity (Reynhout et al.,  
92 2019, Bakke et al., 2021). However, two additional contrasting patterns of glacier  
93 fluctuations have been observed recently. In the Darwin Cordillera (southernmost Patagonia),

94 Reynhout et al. (2021) provided the first  $^{10}\text{Be}$  moraine chronology that shows a maximum  
95 Holocene extent during the last millennium corroborating the radiocarbon-dating-based  
96 results from previous studies by Hall et al. (2019), while on the Antarctic Peninsula, a  
97 maximal glacier advance was recorded during the Mid-Holocene (8 – 4 ka; Kaplan et al.,  
98 2020).

99 These asynchronous fluctuation patterns challenge the concept of a homogeneous Holocene  
100 glacier evolution within the southern mid-latitudes and raise the question whether regional  
101 rather than hemispheric climatic variations have driven glacier behavior during the Holocene.  
102 While CRE glacial paleorecords are increasingly numerous in Patagonia and New Zealand,  
103 the knowledge on glacier fluctuations in other parts of the southern mid-latitudes remains  
104 fragmented. To fill this gap, the Kerguelen Archipelago (49°S, 69°E) provides a precious  
105 sentinel in the Southern Indian Ocean to reconstruct glacier evolution (Fig. 1). Indeed,  
106 Kerguelen is the largest still glaciated sub-Antarctic archipelago of the southern mid-latitudes  
107 (Favier et al., 2016), where several terrestrial moraines are preserved and can be dated.  
108 Therefore, establishing a meaningful glacier chronology at Kerguelen is of major interest, as  
109 it improves our knowledge of glacier fluctuations at the regional southern mid-latitudes scale  
110 within the larger scope of the Southern Hemisphere.

111 Existing studies on Kerguelen glaciers document their fluctuations from Marine Isotopic  
112 Stage 3 (MIS-3; 60 – 25 ka) to the last millennium (section 2.2; Jomelli et al., 2017, 2018;  
113 Charton et al., 2020; Verfaillie et al., 2021). However, knowledge of the evolution of glaciers  
114 at Kerguelen from the end of the Late Glacial (19.0 – 11.7 ka) to the Late Holocene (4 - 0 ka)  
115 remains limited. Several discrete radiocarbon ages from peatland (Frenot et al., 1997)  
116 revealed by modern recession of the Ampere Glacier suggest that this glacier was at least as  
117 small as it is currently during several millennia of the Holocene. Therefore, the aim of this  
118 study is to address the paucity of Late Glacial and Holocene glacier constraints at Kerguelen,

119 using  $^{36}\text{Cl}$  CRE dating on samples of all lithologies, complemented by  $^{10}\text{Be}$  and  $^{26}\text{Al}$  CRE  
 120 analyses on quartz-bearing syenite samples. To do so, we targeted glacial landforms whose  
 121 position and glacial context in the landscape may provide information on Late Glacial and  
 122 Holocene glacier fluctuations (section 2.3). Based on the combination of these two dating  
 123 methods and a Bayesian approach explained in section 3, we provide an updated Kerguelen  
 124 glacier chronology spanning from the Late Glacial to the last millennium (sections 4 and 5.1),  
 125 which is explored in the context of the other glacier and climate records from the southern  
 126 mid-latitudes (sections 5.2 and 5.3.).  
 127



128 **Figure 1.** Map of the Kerguelen Archipelago with the relevant geology in a simplified form.  
 129 The inset shows its location in the Southern Indian Ocean. The three study areas are framed  
 130 in black, **a.** Val Travers site, **b.** Ampere Glacier site, **c.** Arago Glacier site, for which  
 131 geomorphological maps are presented in Figs. 4, 6 and 7, respectively. (data: Digital  
 132

133 Elevation Model from NASA/METI/AIST/Japan Spacesystems and U.S./Japan ASTER  
134 Science Team, 2019; glacier outlines from the GLIMS database (Raup et al., 2007);  
135 geological units from Ponthus (2018)).

136

137

## 138 2. Study area and geomorphological setting

139 The Kerguelen Archipelago is located in the Southern Indian Ocean, with a total surface area  
140 of 7215 km<sup>2</sup>. These 30-million-year-old islands constitute the emerging part of the large  
141 underwater basaltic Kerguelen Plateau (Giret et al., 2003; Fig. 1). However, the regional  
142 geology varies and the basaltic crust is locally intruded by plutonic rocks of various  
143 compositions, such as on the Rallier du Baty Peninsula, where a large volcano-plutonic  
144 complex contains Qz-bearing syenites, or in the Galliéni Peninsula, which comprises a young  
145 volcano-plutonic complex of less than 1 Ma. The eastern part of the Courbet Peninsula is also  
146 different and is only characterized by quaternary deposits but no flood basalts (Fig. 1).

### 147 2.1. Climate setting

148 Due to its location in the Southern Indian Ocean, the Kerguelen Archipelago is subjected to a  
149 subpolar oceanic climate. The related moist and cool air masses, transported by the Southern  
150 Westerly Winds (SWW), enabled the formation of ice caps and glaciers. The SWW also  
151 drives the Antarctic Circumpolar Current (ACC). The ACC flows eastward between 45°S and  
152 65°S (Sokolov and Rintoul, 2009) and is affected by the bathymetry of the Kerguelen Plateau  
153 (46-63°S, 62-85°E). Kerguelen is located in between the sub-Antarctic Front (SAF) at □  
154 46°S (Solokov and Rintoul, 2009) and the Antarctic Polar Front (APF) at □ 50°S (Park et al.,  
155 2014). Nowadays, Kerguelen receives an average of 800 mm of precipitation per year and the



156 mean annual temperature is about 4.5°C at sea level, as recorded daily since 1951 at the  
157 scientific station of Port-aux-Français (Courbet Peninsula; Fig. 1). Additional observations  
158 have provided information on the spatial variability of the climate in the archipelago  
159 (Verfaillie et al., 2015; Favier et al., 2016). In particular, a strong foehn effect has been  
160 identified, being responsible for five times more precipitation in the western part than in the  
161 eastern part of the archipelago (Verfaillie et al., 2019).

## 162 2.2. Previous studies on glaciers and their fluctuations at Kerguelen

163 The western part of the main Kerguelen island, Grande Terre, hosts the warm-based Cook Ice  
164 Cap (CIC; 1050 m a.s.l.), which covered ~ 400 km<sup>2</sup> in 2020 (Verfaillie et al., 2021). Several  
165 other smaller glaciated areas are also located on the Rallier du Baty Peninsula in the  
166 southwest of the archipelago, on the Gallieni Peninsula in the south, and on the Presqu'île de  
167 la Société de Géographie north of CIC (Fig. 1).

168 Previous studies on Kerguelen based on <sup>36</sup>Cl dating of glacial features revealed that glaciers  
169 began to retreat at ~41 ka ago (Jomelli et al., 2018). Erratic and bedrock surfaces located  
170 farther inland of the island dated to ~29-24 ka suggest that large expanses of ice were still  
171 present at that time. Glaciers receded probably until about 15 ka ago. The general glacier  
172 recession during the Late Glacial period was interrupted likely during the Antarctic Cold  
173 Reversal (ACR; 14.5 -12.9 ka), as indicated by <sup>36</sup>Cl dating of three moraines at different  
174 locations – *i.e.* the Bontemps moraine at 13.6 ± 1.5 ka, Belvedere moraine at 15.5 ± 1.8 ka  
175 and G1 moraine of Gentil glacier at 14.3 ± 2.3 ka (Jomelli et al., 2017, 2018; Charton et al.,  
176 2020). A Late Holocene advance is recorded on the debris-covered Gentil Glacier at 2.62 ±  
177 0.97 ka, located at the base of Mount Ross (the highest summit on Kerguelen; 1850 m a.s.l.)  
178 (Charton et al., 2020). Finally, <sup>36</sup>Cl ages from moraines deposited by Ampere Glacier, an  
179 outlet glacier of CIC, reveal - albeit with some scatter - the occurrence of at least two

180 advances of the Ampere Glacier during the last millennium (Jomelli et al., 2017; Verfaillie et  
181 al., 2021). One is attributed to the beginning of the Little Ice Age (Solomina et al., 2016), and  
182 used to constrain a glaciological model that simulated the extent of the Cook Ice Cap during  
183 this period (Verfaillie et al., 2021).

184 Since the 1960s, glaciers at Kerguelen have experienced dramatic wastage, with the surface  
185 area of the CIC expected to disappear by 2100 CE (Verfaillie et al., 2021). This is explained  
186 by decreasing precipitation mainly attributed to the high index Southern Annular Mode  
187 (SAM+) (Thompson et al., 2011; Verfaillie et al., 2015; Favier et al., 2016) and to the long-  
188 term increase in atmospheric temperatures (Verfaillie et al., 2021). Mass and energy balance  
189 conducted on the CIC reveals that temperature impacts the precipitation phase and the  
190 equilibrium line altitude, through changes in the elevation of the 0°C isotherm and therefore  
191 of the rain/snow limit with impacts on both the snow accumulation amount and the glacier  
192 surface albedo (Favier et al., 2016).

### 193 2.3. Study sites and sampling strategy

194 Three sites hosting datable geomorphological features (i.e. moraines, glacially-polished  
195 bedrock and erratics) that are estimated to belong to the Late Glacial and/or the Holocene,  
196 based on a comparison with existing data elsewhere on the islands, were chosen: the Val  
197 Travers valley, Ampere Glacier and Arago Glacier (Fig. 1). Moraines were labelled with  
198 numbers in ascending order from the oldest to the youngest.

199 The Val Travers site (Fig. 1) is characterized by extended U-shaped valleys that were incised  
200 into the basaltic substratum by the eastern outlet glaciers of the CIC. It lies about 10 km  
201 upstream of Bontemps Lake (Fig. 4). We sampled the only two preserved terrestrial moraines  
202 found in the valley (V1 and V2), which may have been formed by a branch of the Explorateur

203 Glacier (Fig. 4). Four samples (VLT-10, -11, -12, and -13) were taken at 62 m a.s.l from the  
204 V1 moraine ridge, which is located at 14.2 km from the present-day frontal area of the eastern  
205 glaciers of the CIC (Fig. 4). Five moraine boulders (VLT-05, -06, -07, -08, and -09) were  
206 sampled at 73 m a.s.l. on the V2 moraine, which was deposited about 1.5 km upstream of the  
207 V1 moraine (Figs. 2a and 4). Finally, one sample (VLT-04) was extracted from a polished  
208 bedrock surface, located on the right-lateral plateau near Mount A. Gampert at an elevation of  
209 437 m a.s.l. and at a distance of about 9 km downstream of the V1 moraine (Figs. 2a and 4).  
210 All boulders sampled at this site have a basaltic lithology.

211 The Ampere Glacier is a lake-terminating outlet glacier of the CIC, which flows south-east of  
212 the ice cap on the basaltic substratum (Fig. 1). Currently, the Ampere Glacier (67 km<sup>2</sup> in  
213 2011) is 12 km long (Berthier et al., 2009; Verfaillie et al., 2021) with a large proglacial lake.  
214 The Ampere's proglacial margin (9 km long) is characterized by an outwash plain that  
215 reaches Table Bay, with a set of six moraines between about 3.5 and 7 km from the current  
216 ice front (Figs. 1 and 6). Eleven new basaltic samples, i.e. six erratic boulders (MO-03, -04, -  
217 06, -08, -11, and -12) and five bedrock samples (MO-02, -05, -07, -09, and -13) were taken  
218 uphill (between 120 and 290 m a.s.l.) on the southern part of the shore of the Ampere Lake at  
219 distances ranging from 1.5 to 2.8 km from the glacier's snout (Figs. 2b and 6). Each sampled  
220 bedrock surface is paired with at least one erratic (Figs. 2b and 6). These erratic boulders are  
221 aligned in a lateral continuum of the frontal moraine sequence.

222 The south-west part of the archipelago hosts the Rallier du Baty Peninsula (Fig. 1), an  
223 alkaline volcano-plutonic complex, which mostly consists of syenites with rock  
224 crystallization ages ranging from about 12 Ma to 8 Ma (Ponthus et al., 2020). More recent  
225 lava flows, composed of trachytes, are also present, resulting from volcanic activity between  
226 ~1.15 Ma (Dosso et al., 1979) and the last millennium (900-1000 CE) (Guillaume Delpech,

227 personal communication). Rallier du Baty Peninsula is covered by a small ice cap, with  
228 several land-terminating outlet glaciers. Among them, the Arago Glacier, which peaks at  
229 1262 m a.s.l., is a 6 km long lake-terminating glacier and flows down on the eastern slope of  
230 Mont Henri, towards the east into the Larmor valley (Figs. 1 and 7). The only moraine (A1)  
231 so far detected at a distal location (11 km) from the current glacier front, is composed of  
232 syenite boulders. Six syenite samples (RDB-23, -24, -25, -26, -27, and -28) were taken at 72  
233 m a.s.l. on this outermost A1 moraine (Figs. 2c and 7). Closer to the glacier front, a sequence  
234 of four moraines mainly composed of volcanic rocks (trachyte) was identified, but only two  
235 of them (the most distant from the current front) were chosen for dating: A2a and A2b (Fig.  
236 7). They were formed alongside the moraine-dammed lake at about 3 km from the current  
237 glacier front. From the crest of the frontal moraine A2a, four samples (RDB-01, -02, -04, and  
238 -05) were taken at 80 m a.s.l., all being syenites (Fig. 7). Another three samples of trachytic  
239 composition (RDB-15, -17, and -18) were collected from the ridge of the lateral moraine A2b  
240 at 157 m a.s.l. (Figs 2d and 7). In addition, one glacially-polished syenite bedrock sample  
241 (RDB-13) was taken at an average elevation of 60 m a.s.l. on the right-lateral flank of the  
242 valley, located at about 5 km upstream of A1 moraine (Fig. 7).



243  
 244 **Figure 2.** **a.** Photograph of Val Travers site showing V2 moraine and the bedrock surface. **b.**  
 245 shows a view of Ampere proglacial margin towards Table Bay presenting the sampled paired  
 246 bedrock surfaces and perched erratic boulders. **c.** and **d.** are photographs of A1 moraine and  
 247 A2b moraine, respectively, located on Arago Glacier forefield.

248 3. Methods

249 3.1. Sampling

250 Sampling was carried out during a field campaign in 2017-2018. In total, 34 samples from  
 251 glacially-polished bedrock, moraine boulders and erratic boulders were collected (Table 1). A  
 252 hammer and chisel were used to extract the uppermost 2-3 cm of moraine boulder surfaces,  
 253 erratic boulders and bedrock (Fig. 2). Particular attention was paid to sample flat and non-  
 254 weathered surfaces. The geographic coordinates and elevations were recorded with a  
 255 handheld GPS device and topographic shielding was measured in the field with a clinometer.

256 3.2. *In situ* cosmogenic nuclide dating

257 For CRE dating *in situ*  $^{36}\text{Cl}$  is the most suitable cosmogenic nuclide, because Kerguelen's  
258 volcanic lithology contains Ca, K, Ti, Fe, and Cl, which are the main target elements for  
259 analysis with this method. We also conducted  $^{10}\text{Be}$  measurements on samples that allowed  
260 the isolation of sufficient quartz. In addition, we measured  $^{26}\text{Al}$  in these samples with the aim  
261 to verify if the sampled surfaces have been affected by some inheritance from the last  
262 interglacial (long-term exposure-burial) or by recent exhumation.

### 263 3.2.1 Chemical procedures

264 Sample preparation for *in situ*-produced  $^{36}\text{Cl}$ ,  $^{10}\text{Be}$  and  $^{26}\text{Al}$  CRE dating was performed in the  
265 “Laboratoire National des Nucléides Cosmogéniques” (LN<sub>2</sub>C) at CEREGE, Aix-en-provence,  
266 France. Samples were crushed and sieved to collect the 250-500  $\mu\text{m}$  fraction.

267 All samples but one (RDB-13) presented in this study were dated with  $^{36}\text{Cl}$ . Basaltic and  
268 trachytic whole-rock samples were processed according to routine procedures using a method  
269 similar to Schimmelpfennig et al. (2011). The low abundance of phenocrysts in these rocks  
270 required the use of the whole-rock fractions for these samples, as in the previous studies in  
271 the Kerguelen Islands (Jomelli et al., 2017, 2018; Charton et al., 2020; Verfaillie et al., 2021).  
272 Aliquots of bulk rocks were selected for analyses of major and trace element concentrations  
273 at the Service d'Analyse des Roches et des Minéraux (SARM, Nancy, France) (Table 2).  
274 Major and trace elements are needed to evaluate the contribution of the capture of low-energy  
275 neutrons on  $^{35}\text{Cl}$  and the nucleogenic production to the total  $^{36}\text{Cl}$  production. Exposure dating  
276 of syenites from Rallier du Baty represented a considerable experimental effort, as they have  
277 never been processed before for  $^{36}\text{Cl}$  or other cosmogenic nuclides at the LN<sub>2</sub>C laboratory.  
278 All syenite samples are dominated by alkali feldspars (Na and K-rich) with minor amounts of  
279 quartz and other magnetic minerals (mainly amphiboles and pyroxenes). Because the  
280 feldspars were expected to have low amounts of natural Cl and they are the dominant non-

281 magnetic mineral phase, they were separated for chemical  $^{36}\text{Cl}$  extraction from the magnetic  
282 minerals in the syenite samples (RDB-01, -02, -05, -23, -24, -25, -26, -27 and -28) using a  
283 Frantz magnetic separator. We then leached all samples with a HF/HNO<sub>3</sub> (Ultrapur) acid  
284 mixture with the aim to eliminate atmospheric  $^{36}\text{Cl}$  and other potentially Cl-rich mineral  
285 phases (Schimmelpfennig et al., 2009). This step removed ~10-20% of the initial feldspar-  
286 dominated fractions and ~40% of the initial whole rock sample. Another 2 g aliquot of the  
287 rinsed and dried grains for each sample was sent to SARM for major element analyses by  
288 ICP-OES, which provides the concentrations of the target elements (*i.e.* Ca, K, Ti and Fe) for  
289  $^{36}\text{Cl}$  production by spallation and slow muon capture (Table 3). The final dissolution of the  
290 sample grains was performed in a HF/HNO<sub>3</sub> (Ultrapur) acid mixture after addition of a  $^{35}\text{Cl}$ -  
291 enriched spike (~99%) for isotope dilution (Ivy-Ochs et al., 2004). In total, 6 chemistry  
292 blanks (Bk 5, Bk 7, Bk 8, Bk 10, Bk 11 and Bk 12) were processed together with the samples  
293 (one with each sample batch, see Table 4 for detailed information). The remaining steps  
294 follow the method presented in Schimmelpfennig et al. (2011). Prior to AMS measurements,  
295 AgCl targets were pressed into nickel cathodes.  $^{36}\text{Cl}/^{35}\text{Cl}$  and  $^{35}\text{Cl}/^{37}\text{Cl}$  ratio measurements  
296 were performed by Accelerator Mass Spectrometry (AMS) at the French AMS national  
297 facility (ASTER) after normalization to the inhouse standard SM-CL-12, using an assigned  
298 value of  $1.428 (\pm 0.021) \times 10^{-12}$  for the  $^{36}\text{Cl}/^{35}\text{Cl}$  ratio (Merchel et al., 2011) and assuming a  
299 natural ratio of 3.127 for the stable ratio  $^{35}\text{Cl}/^{37}\text{Cl}$ . From these measurements the  $^{36}\text{Cl}$  and Cl  
300 concentrations were calculated, using the principles of isotope dilution and following the  
301 equations in Schimmelpfennig (2009). All concentrations were blank-corrected by  
302 subtracting the number of atoms Cl and  $^{36}\text{Cl}$  of the batch-specific blank from those of the  
303 corresponding samples, respectively (Table 4). An error propagation calculation was  
304 performed following the standard procedures given in Taylor (1997).

305 All syenite samples were inspected for the amount of quartz they contained. Eight samples  
306 were estimated to have at least 1% of quartz, which was isolated from the magnetic minerals  
307 by magnetic separation (using a Frantz magnetic separator) and from K-feldspars by  
308 densimetric separation using heavy liquids. The quartz fraction was leached several times  
309 using a diluted HF acid mixture in an ultrasonic bath to remove any remaining feldspars and  
310 to eliminate atmospheric  $^{10}\text{Be}$  from the quartz grains. Finally, only three samples (RDB-13, -  
311 24 and -27) yielded sufficient amounts of quartz for  $^{10}\text{Be}$  and  $^{26}\text{Al}$  chemical procedures (~12-  
312 52 g from at least 4 kg of crushed rock). As RDB-13 was collected from a quartz-enriched  
313 vein, it yielded the highest amount of quartz (~52 g). The total dissolution of the samples was  
314 then performed in a concentrated HF solution after the addition of 150  $\mu\text{l}$  of an in-house  $^9\text{Be}$   
315 carrier solution ( $3025 \pm 9$  ppm; Merchel et al., 2008). An aliquot of the solution was taken  
316 after complete digestion of the samples to quantify the total Al concentration by ICP-OES  
317 analysis. Due to the presence of high amounts of natural  $^{27}\text{Al}$  in the processed fraction  
318 (probably due to small residues of feldspars), no  $^{27}\text{Al}$  carrier was added to the aliquot.  
319 Beryllium and aluminum were extracted using anion and cation exchange columns and  
320 alkaline precipitation. Afterwards, samples were oxidized at 700°C for 1 hour and the final  
321  $\text{BeO}$  and  $\text{Al}_2\text{O}_3$  were mixed with niobium and silver powders respectively, and loaded into  
322 copper cathodes. AMS measurements of the  $^{10}\text{Be}/^9\text{Be}$  ratios were conducted at the French  
323 national AMS facility (ASTER) (Arnold et al., 2010). Samples were calibrated against the in-  
324 house standard STD-11 ( $^{10}\text{Be}/^9\text{Be} = 1.191 \pm 0.013 \times 10^{-11}$ ; Braucher et al., 2015) and using a  
325  $^{10}\text{Be}$  half-life of  $1.387 (\pm 0.0012) \times 10^6$  years (Chmeleff et al., 2010; Korschinek et al., 2010).  
326 Aluminum measurements were performed against an in-house standard SM-Al-11 with  
327  $^{26}\text{Al}/^{27}\text{Al} = (7.401 \pm 0.064) \times 10^{-12}$  which has been cross-calibrated against the primary  
328 standards certified by a round-robin exercise (Mерchel and Bremser, 2004). Analytical  
329 uncertainties include ASTER counting statistics and stability, the latter amounting to ~0.5%



330 for  $^{10}\text{Be}$  (Arnold et al., 2010).  $^{10}\text{Be}$  measurements were corrected for blank background by  
331 subtracting the number of atoms  $^{10}\text{Be}$  of the blank from those of the samples (Table 5).

332

### 333 3.2.2. CRE age calculations

334 The  $^{36}\text{Cl}$  CRE age calculations were performed using the Excel® spreadsheet published by  
335 Schimmelpfennig et al. (2009), following the methods used in the previous Kerguelen studies  
336 (Jomelli et al., 2017, 2018; Charton et al., 2020; Verfaillie et al., 2021). The calculator takes  
337 into account all  $^{36}\text{Cl}$  production reactions (spallation of the target elements Ca, K, Ti and Fe,  
338 slow muon capture by Ca and K, capture of cosmogenic low-energy (*i.e.* thermal and  
339 epithermal) neutrons by  $^{35}\text{Cl}$  and nucleogenic production) and provides in detail their relative  
340 contributions (Supplemental Material Table 1), based on the sea level and high latitude  
341 (SLHL) production rates, scaling factors, sample chemical composition (Tables 2 and 3),  
342 sample thickness, topographic shielding, and rock formation age (Table 1). The time-  
343 invariant “St” scaling (Stone, 2000) was used for the calculation of all samples. As no local  
344 production rates exist for the Kerguelen Archipelago, the following  $^{36}\text{Cl}$  SLHL production  
345 rates, mostly calibrated at mid-latitude sites and previously applied in Kerguelen, were used  
346 for the calculations:  $42.2 \pm 4.8$  atoms of  $^{36}\text{Cl}$  (g Ca) $^{-1}$  yr $^{-1}$  for Ca spallation (Schimmelpfennig  
347 et al., 2011),  $148.1 \pm 7.8$  atoms of  $^{36}\text{Cl}$  (g K) $^{-1}$  yr $^{-1}$  for K spallation (Schimmelpfennig et al.,  
348 2014),  $13 \pm 3$  atoms of  $^{36}\text{Cl}$  (g Ti) $^{-1}$  yr $^{-1}$  for spallation of Ti (Fink et al., 2000),  $1.9 \pm 0.2$  atoms  
349 of  $^{36}\text{Cl}$  (g Fe) $^{-1}$  yr $^{-1}$  for Fe spallation (Stone et al., 2005), and  $696 \pm 185$  neutrons (g air) $^{-1}$  yr $^{-1}$   
350 for the rate of epithermal neutron production from fast neutrons in the atmosphere at the  
351 Earth/atmosphere interface (Marrero et al., 2016). We applied a value of  $160 \text{ g cm}^{-2}$  for the  
352 high-energy neutron attenuation length and  $2.4 \text{ g cm}^{-3}$  for the bulk rock density. The two  $^{36}\text{Cl}$   
353 production reactions induced by capture of low-energy neutrons on  $^{35}\text{Cl}$  are hard to quantify,

354 as the low-energy neutron flux depends on the rock composition and environmental factors,  
355 such as snow cover and presence of water (Zreda et al., 1993; Phillips et al., 2001;  
356 Schimmelpfennig et al., 2009; Zweck et al., 2013; Dunai et al., 2014). We therefore attributed  
357 a 30% uncertainty to the  $^{36}\text{Cl}$  production from capture of cosmogenic low-energy neutrons by  
358  $^{35}\text{Cl}$  reaction production, based on empirical and model experiments (Zreda et al., 1993;  
359 Schimmelpfennig et al., 2009; Zweck et al., 2013; Dunai et al., 2014; Marrero et al., 2016).  
360 The estimation of the nucleogenic  $^{36}\text{Cl}$  contribution in the spreadsheet follows the  
361 calculations provided by Phillips and Plummer (1996). The nucleogenic  $^{36}\text{Cl}$  production is  
362 induced by low-energy neutron capture on  $^{35}\text{Cl}$ , but in this case the low-energy neutrons  
363 result from spontaneous fission of  $^{238}\text{U}$  and reactions of alpha-particles generated during U  
364 and Th decay. The calculation method further assumes that nucleogenic  $^{36}\text{Cl}$  production starts  
365 with the rock formation (crystallization) and is not preserved during magmatic processes  
366 (Gosse and Phillips, 2001; Schimmelpfennig et al., 2009; Sarikaya et al., 2018; Anjar et al.,  
367 2021). After ~1-2 Ma, nucleogenic  $^{36}\text{Cl}$  production and decay (half-life of  $^{36}\text{Cl}$ : 301 ka) are in  
368 equilibrium, which makes the nucleogenic  $^{36}\text{Cl}$  contribution sensitive to differences in the  
369 formation ages only if they are <1 Ma (Sarikaya et al., 2018). Most rock samples in our  
370 dataset have formation ages that are much older than 1 Ma (Table 1; Guillaume Delpech,  
371 personal communication). The nucleogenic  $^{36}\text{Cl}$  production is therefore in equilibrium with  
372  $^{36}\text{Cl}$  decay. Only samples from a recent lava flow on Arago Glacier site (samples RDB-01, -  
373 02, -04, -05, -15, -17 and -18) have a young formation age of ~10 ka or less (Guillaume  
374 Delpech, personal communication; Table 1), i.e. the nucleogenic  $^{36}\text{Cl}$  contribution is much  
375 lower than in the older samples. Further, calculations of the nucleogenic  $^{36}\text{Cl}$  production in  
376 the spreadsheet developed by Schimmelpfennig et al. (2009) are based on the assumption that  
377 the nucleogenic flux of neutrons is homogenous within the bulk rock. Thus, the bulk rock  
378 composition in U and Th is commonly used to estimate the nucleogenic production of  $^{36}\text{Cl}$  in

379 our samples. This assumption is valid when dating volcanic material because the fast cooling  
380 of the lava commonly induces little crystallization with the sparse occurrence of bigger  
381 phenocrysts in the matrix. In the case of Kerguelen, the basalts and trachytes used in this  
382 study are mostly aphyric or have a microlitic porphyric microstructure with only a few  
383 percent of phenocrysts. On the contrary, the plutonic syenite samples of our dataset have a  
384 coarse-grained microstructure and are composed of large crystals (up to centimeter size),  
385 frequently including small inclusions of accessory minerals (hundreds of microns or less)  
386 with highly variable U and Th concentrations (eg. zircon, monazite). It is therefore plausible  
387 that the nucleogenic neutron flux is not homogeneous in the syenites samples due to the  
388 occurrence of accessory minerals in some larger crystals. In order to prevent a bias in the  
389 estimation of the nucleogenic production for the plutonic samples, we thus used the U and Th  
390 compositions of the feldspar-dominated fractions separated instead of the U-Th  
391 concentrations of the bulk fraction because the  $^{36}\text{Cl}$  analysis was performed on these feldspar  
392 separates. We assign a formal uncertainty of 5% to the nucleogenic  $^{36}\text{Cl}$  production, as to our  
393 knowledge no specific investigations have been conducted on the uncertainties inherent to the  
394 commonly-used calculation approach. In the Excel® spreadsheet, all uncertainties are  
395 propagated throughout to the final  $^{36}\text{Cl}$  exposure age following the standard procedures given  
396 in Taylor (1997).

397  $^{10}\text{Be}$  CRE ages were calculated with the online CREp program (Martin et al., 2017;  
398 <http://crep.crpq.cnrs-nancy.fr>) and are listed in Table 5. Scaling to the sample locations was  
399 made according to the time-dependent version of the Stone (2000) scaling (Martin et al.,  
400 2017), with the ERA40 atmosphere (Uppala et al., 2005) and the atmospheric  $^{10}\text{Be}$ -based  
401 VDM geomagnetic database (Muscheler et al., 2005). The production rate used to compute  
402 the  $^{10}\text{Be}$  ages is regional “southern mid-latitudes” mean based on three calibration sites  
403 located in Patagonia (Kaplan et al., 2011) and New-Zealand (Putnam et al., 2010b), as

404 available in the online ICE-D dataset (Martin et al., 2017; <http://calibration.ice-d.org/>). Using  
405 the Stone time-dependent scaling in CREp, this regional mean  $^{10}\text{Be}$  production rate  
406 corresponds to a sea level high latitude (SLHL) value of  $4.05 \pm 0.04$  atoms  $\text{g}^{-1} \text{yr}^{-1}$ . Note that  
407 this value is only 1.5% lower than the global average computed with all available worldwide  
408 calibration sites (Martin et al., 2017).

409 No correction was made for snow cover nor denudation for both the  $^{36}\text{Cl}$  and  $^{10}\text{Be}$  age  
410 calculations, in line with previously published  $^{36}\text{Cl}$  ages from Kerguelen. Current seasonal  
411 snow cover corresponds to a thickness of maximum 10 cm, during durations of about 1.5  
412 months at 90 m a.s.l. and 3 weeks at 35 m a.s.l. (Verfaillie et al. 2015; Favier et al. 2016).  
413 Such cover would correspond to a correction lower than 2 % (Delunel et al., 2014) and can  
414 hence be safely neglected. Similarly, given the exposure timescale ( $< 20$  ka), the impact of  
415 denudation is probably lower than the analytical uncertainties by denudation processes.

416 The resulting  $^{36}\text{Cl}$  and  $^{10}\text{Be}$  CRE ages are listed in Table 4 and 5 with their inferred  $1 \sigma$   
417 uncertainties (*i.e.* the total uncertainties which take into account the analytical and production  
418 rate uncertainties) and their analytical uncertainties in brackets. Surface exposure ages are  
419 also plotted and shown in Figs. 4, 6 and 7. In the main text and on the figures, we indicate the  
420 individual ages with their total uncertainties, whereas probability density curves of individual  
421 ages are presented with analytical uncertainties only to allow internal comparison (Figs. 3, 5  
422 and 9). For a given site, the obtained ages from a single object (moraine, erratic) were  
423 compared using a  $\text{Chi}^2$  test, and 95% outliers were then removed (Ward and Wilson, 1978).  
424 Then, in line with former Kerguelen studies, we computed the arithmetic mean  $^{36}\text{Cl}$  age for  
425 each object (reported with their total uncertainties in Table 4). All exposure ages are  
426 expressed in yr until 1 ka, and in ka for older ages.

427

### 428 3.3. Bayesian modeling

429

430 To reduce the dating uncertainties, we exploited the stratigraphic relationships between the  
431 dated glacial objects and applied a Bayesian filter on a part of our  $^{36}\text{Cl}$  moraine age dataset  
432 (Cooley et al., 2006; Naveau et al., 2007; Parnell, 2011), following an approach previously  
433 developed (Blard et al., 2013; Martin et al., 2018). In practice, we first computed a synthetic  
434 probability density function (pdf) for each moraine, summing the individual pdf of all  
435 individual  $^{36}\text{Cl}$  ages  $f_{\text{Sample}}$ :

436

$$437 \quad f_{\text{Moraine}}(t) = \frac{1}{n} \sum_{i=1}^n f_{\text{Sample}} \quad (1)$$

438

439 Then, the pdf of ages of moraines that are in successive stratigraphic order were processed  
440 using Bayesian filtering. Including these stratigraphic observations permitted to refine the pdf  
441 of both younger and older moraines, considering that a distal moraine is necessarily older  
442 than a proximal one (Martin et al., 2018). Filtered pdf,  $f^*$  of older and younger moraines, are  
443 computed according to Equations (2) and (3), respectively:

444

$$445 \quad f_{\text{Older Moraine}}^*(t) = f_{\text{Older Moraine}}(t) \times \int_0^t f_{\text{Younger Moraine}}(\tau) d\tau \quad (2)$$

446

$$447 \quad f_{\text{Younger Moraine}}^*(t) = f_{\text{Younger Moraine}}(t) \times \int_t^\infty f_{\text{Older Moraine}}(\tau) d\tau \quad (3)$$

448

449 This filtering is useful to reduce the total dating uncertainties arising from geological  
450 dispersions (erosion or inheritance). In practice, the vicinity of the successive moraines of  
451 this dataset implied that this filtering was only applied to moraines V1 and V2 of Val Travers  
452 (this study; Fig. 3) and moraines M1 and M2 of Ampere ( $^{36}\text{Cl}$  ages were first published in

453 Jomelli et al. (2017) and Verfaillie et al. (2021); Fig. 5). It was indeed unnecessary to apply  
454 this filtering to other moraine couples, because the corresponding  $^{36}\text{Cl}$  ages are too distant.

455

### 456 3.4. Review of existing Holocene cosmogenic data

457

458 We aim to compare the updated Kerguelen glacial chronologies to those from other southern  
459 mid-latitude regions. To address this issue, we focused on studies devoted to alpine glaciers,  
460 from the alpine ICE-D database (<http://alpine.ice-d.org/>), which compiles cosmogenic nuclide  
461 exposure ages (mostly  $^{10}\text{Be}$ ) from alpine glacier sites around the world. We preferentially  
462 target moraine datasets providing direct dating of the main advances of a glacier. Available  
463 data from southern mid-latitude glacier chronologies (n=14) were tabulated as follows: (i)  
464 moraine mean ages with their inferred internal uncertainties were attributed to one of the  
465 subperiods of the Holocene (Early, Mid- or Late Holocene) based on the nominal age and (ii)  
466 we only selected the glacial chronologies for which the entire sequence of Holocene moraines  
467 in the valley were preserved and dated. After age compilation, we identified patterns  
468 according to either the presence or absence of at least one moraine belonging to a specific  
469 subperiod in each valley. The results and interpretation of these patterns are presented in  
470 Supplementary Material Table 2, 3 and 4 and in Fig 8. The class of data is shown as  
471 qualitative histograms. The x-axis of the histograms represents the three sub periods of the  
472 Holocene, namely Early Holocene (11.6 - 8 ka), Mid-Holocene (8 - 4 ka) and Late Holocene  
473 (4 - 0 ka). The height of the bar represents the qualitative appreciation of the length of the  
474 glacier following the stratigraphic principle.

475

476

## 477 4. Results and age interpretation

478

479 4.1.  $^{36}\text{Cl}$  ages from Val Travers site (n=10)

480

481 Samples VLT-10, -11, -12 and -13 from V1 moraine give ages of  $12.6 \pm 1.7$  ka,  $16.0 \pm 2.1$  ka,

482  $16.7 \pm 2.2$  ka and  $14.9 \pm 2.0$  ka respectively and yield a median age of  $16.0 \pm 1.9$  ka after the

483 Bayesian filtering process, (n=4). (Table 4, Fig. 3, Fig. 4).  $^{36}\text{Cl}$  ages of VLT-05, -06, -07, -08

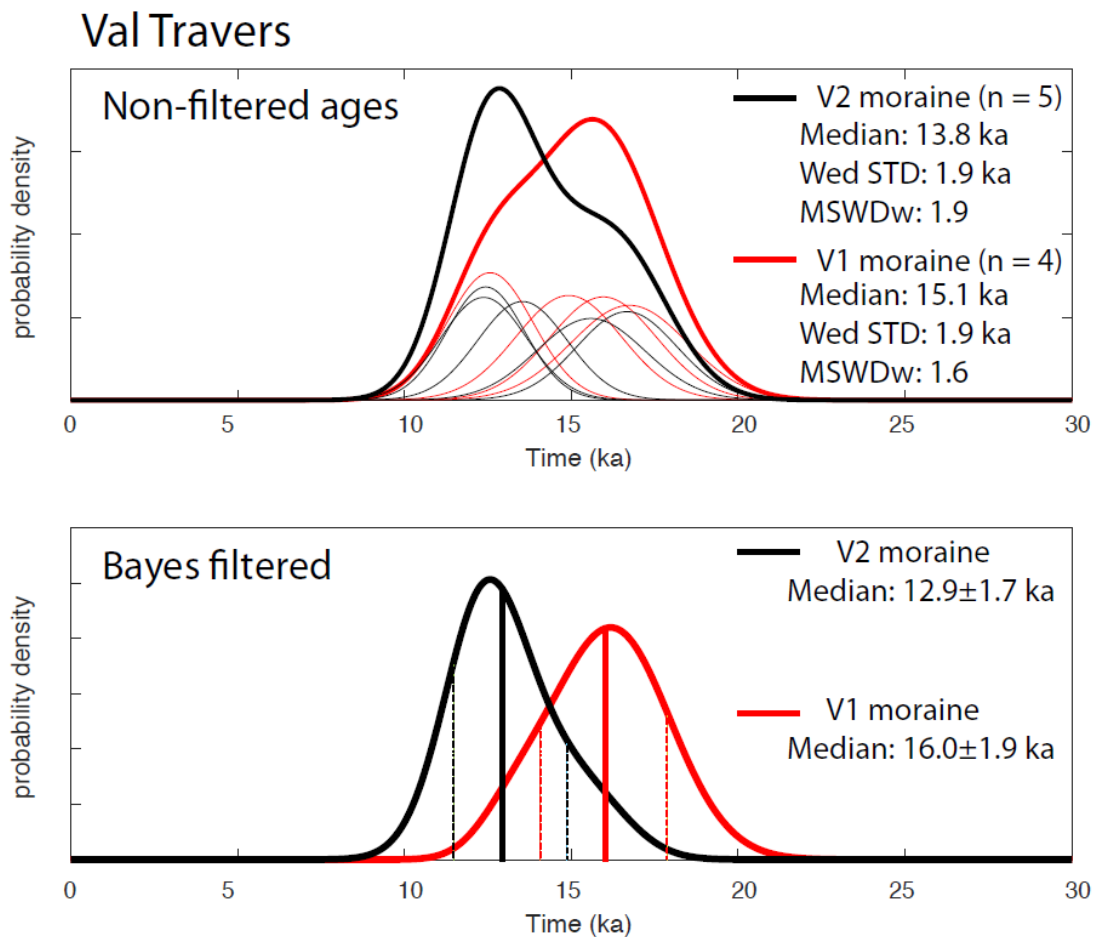
484 and -09, collected on V2 moraine are  $15.6 \pm 2.0$  ka,  $12.4 \pm 1.6$  ka,  $12.4 \pm 1.5$  ka,  $16.7 \pm 2.0$  ka

485 and  $13.5 \pm 1.7$  ka, respectively. The median age and total uncertainty of V2 moraine is  $12.9 \pm$

486  $1.7$  ka (n = 5) (Table 4, Fig. 3, Fig. 4). The  $^{36}\text{Cl}$  age of VLT-04, which was extracted from a

487 bedrock atop the U-shaped valley is  $17.3 \pm 2.2$  ka (Table 4, Fig. 4).

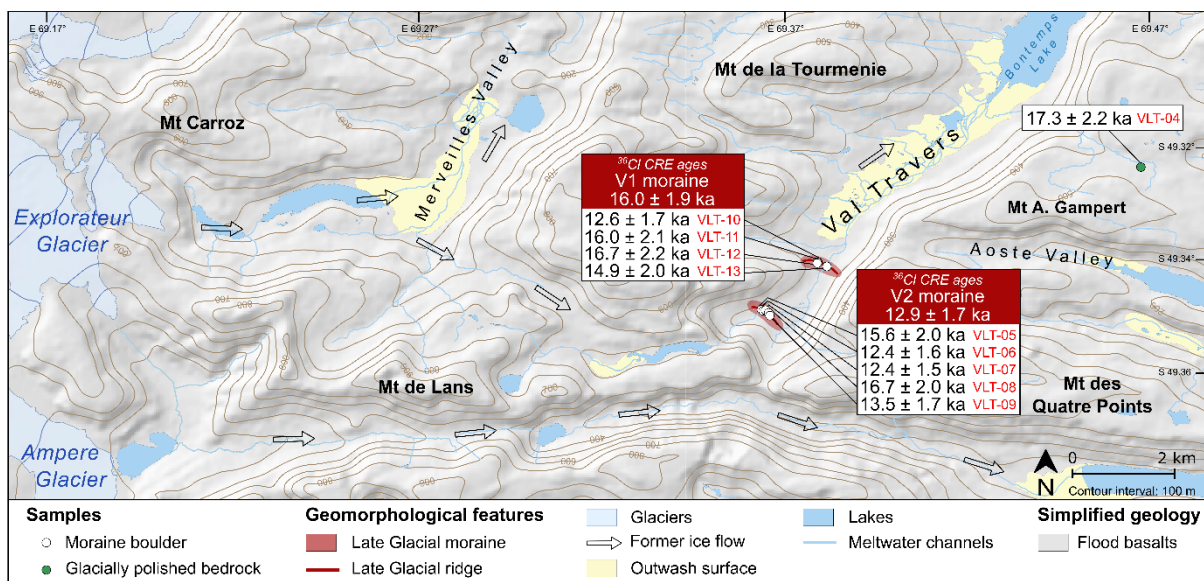
488



489

490 **Figure 3.** Probability plots of  $^{36}\text{Cl}$  boulder CRE ages from V1 (red curves) and V2 (black  
 491 curves) moraines at Val Travers site before the Bayesian filter (upper panel) and after the  
 492 Bayesian filter (bottom panel). Individual ages are represented by Gaussian curves in the  
 493 upper panel, which only include the analytical uncertainties. The summed probability is  
 494 presented by thick curves. Also shown are the statistical parameters for each landform.

495  
 496  
 497  
 498



499  
 500 **Figure 4.** Glacial geomorphological map of the Val Travers site. White boxes show the  $^{36}\text{Cl}$   
 501 sample ages of moraine and bedrock with their analytical uncertainties. The median ages for  
 502 moraine groups are shown in colored boxes with their total uncertainties (i.e. standard  
 503 deviation, analytical and production rate uncertainties).

504

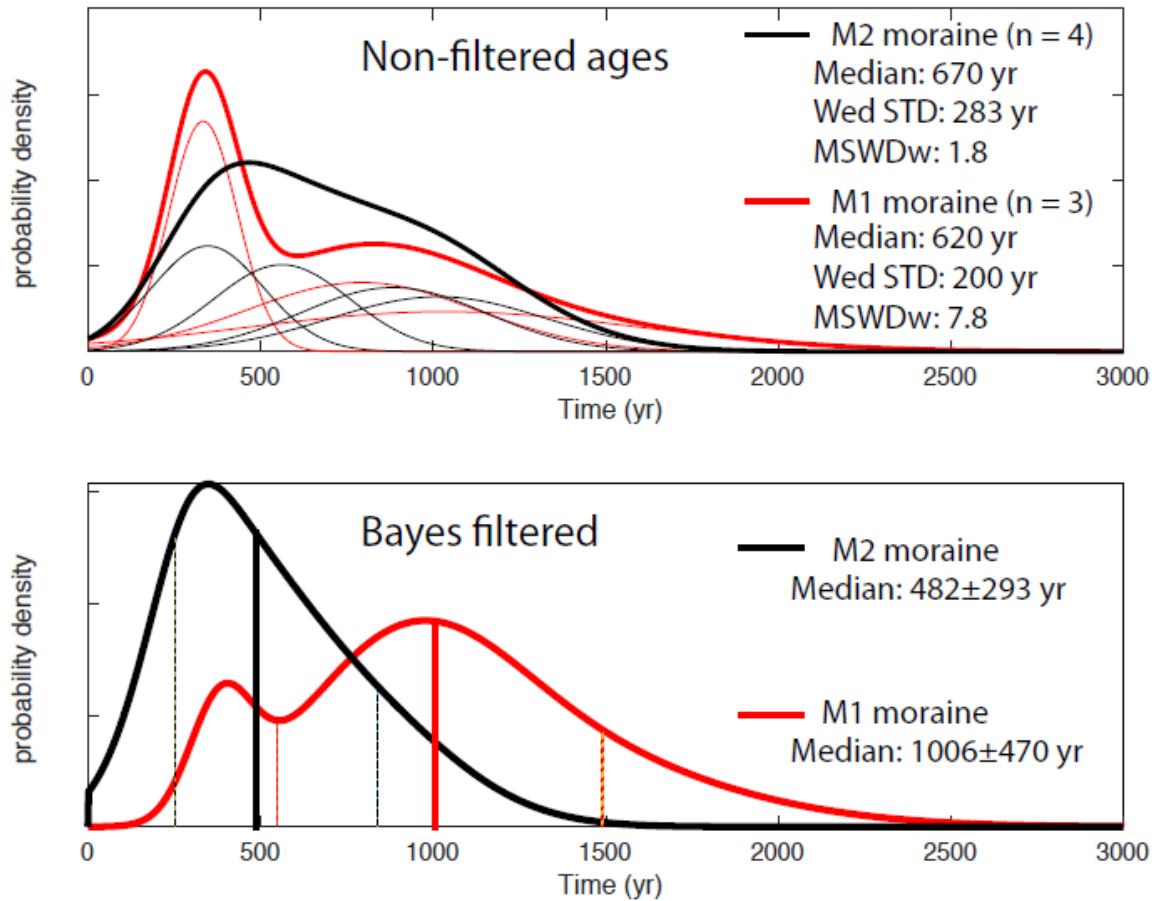
505 4.2.  $^{36}\text{Cl}$  ages from Ampere Glacier site (n= 11)



506 The erratic boulder samples associated with bedrock surfaces, MO-12, -11, -04, -03, -08 and -  
507 06, yield ages of  $290 \pm 140$  yr,  $870 \pm 180$  yr,  $80 \pm 50$  yr,  $680 \pm 340$  yr,  $620 \pm 170$  yr and  $2.37$   
508  $\pm 0.38$  ka, respectively (Table 4, Fig. 6). MO-04 and -06 were identified as outliers based on  
509 the  $\text{Chi}^2$  test and were therefore excluded from the mean age calculation. MO-04 has an age  
510 considered too young probably due to post-depositional rotation or exhumation, whereas the  
511 older age of MO-06 is probably affected by inheritance. The remaining samples MO-12, -11,  
512 -03 and -06 have a mean arithmetic age of  $610 \pm 250$  yr. The bedrock samples MO-13, -05, -  
513 02, -09 and -07 taken from downstream to upstream on the right shore of Ampere Lake yield  
514 ages of  $11.3 \pm 1.6$  ka,  $14.0 \pm 1.8$  ka,  $10.1 \pm 1.3$  ka,  $4.43 \pm 0.59$  ka and  $8.9 \pm 1.1$  ka (Table 4,  
515 Fig. 6). The interpretation of these ages will be discussed in section 5.1. Individual moraine  
516 boulder  $^{36}\text{Cl}$  ages presented in Fig. 6 were first published in Jomelli et al. (2017) and  
517 Verfaillie et al. (2021). The weighted means of M1 and M2 moraines and associated total  
518 uncertainties gave ages of  $800 \pm 260$  yr and  $580 \pm 310$ , respectively. After the Bayesian  
519 filtering process, M1 moraine gives a median age of  $1000 \pm 470$  yr ( $n=3$ ) and M2 moraine  
520 gives a median age of  $480 \pm 290$  yr ( $n=4$ ) (Fig. 5).

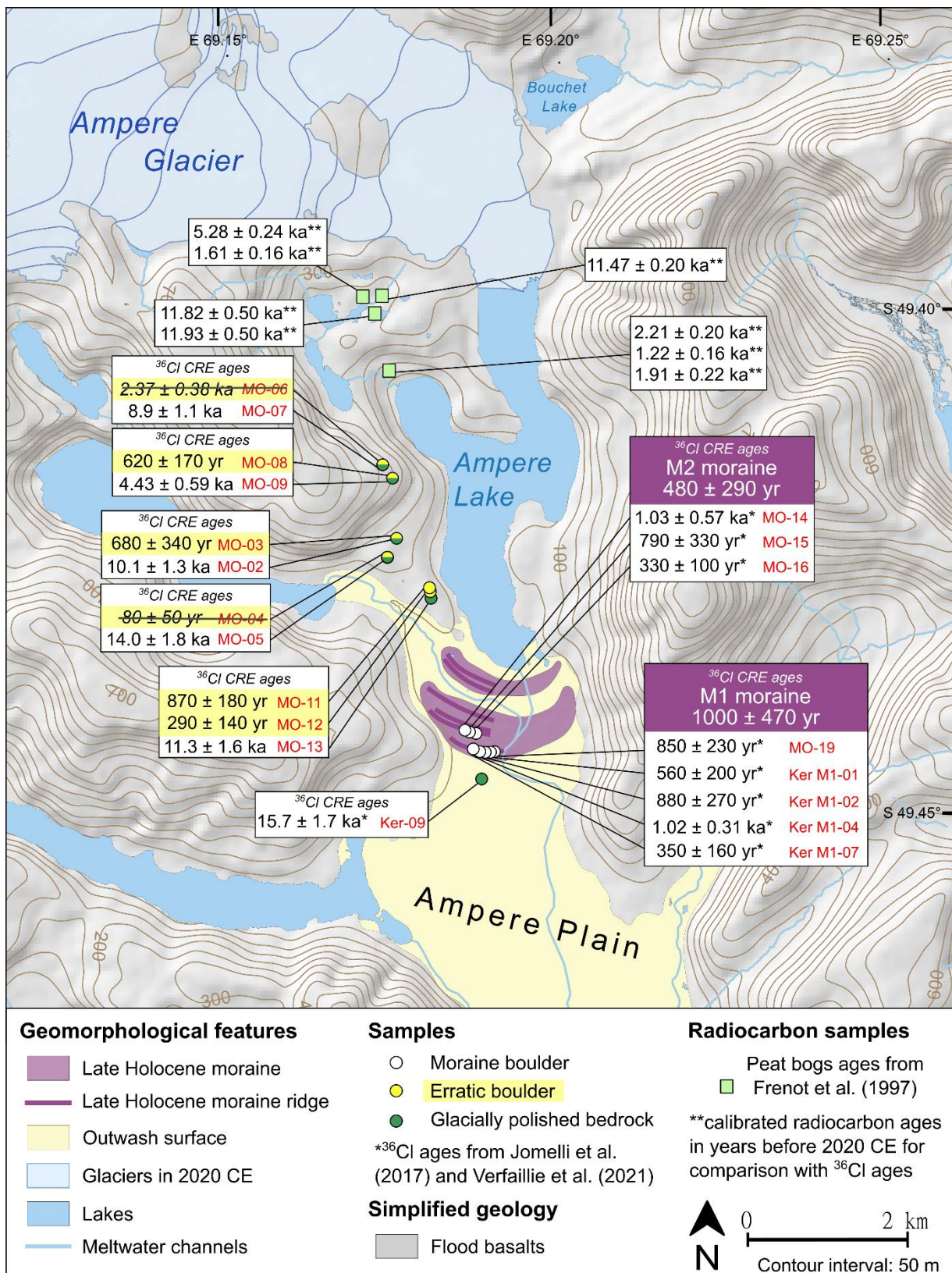
521

## Ampere



522

523 **Figure 5.** Probability plots of  $^{36}\text{Cl}$  boulder CRE ages from M1 (red curves) and M2 (black  
524 curves) moraines at Ampere site ( $^{36}\text{Cl}$  boulder CRE ages were first published in Jomelli et al.  
525 (2017) and Verfaillie et al. (2021)) before the Bayesian filter (upper panel) and after the  
526 Bayesian filter (bottom panel). Individual ages are represented by Gaussian curves in the  
527 upper panel, which only include the analytical uncertainties. The summed probability is  
528 presented by thick curves. Also shown are the statistical parameters for each landform.



529

530 **Figure 6.** Glacial geomorphological map of the Ampere Glacier. White boxes show the <sup>36</sup>Cl

531 sample ages of erratic boulders and bedrock with their inferred analytical uncertainties.

532 Samples written in striked-through italic text are rejected as outliers and therefore excluded

533 from the discussion. Moraine boulder  $^{36}\text{Cl}$  CRE ages are from Jomelli et al. (2017) and  
534 Verfaillie et al. (2021). The median ages for moraine groups are shown in colored boxes with  
535 their total uncertainties (i.e. standard deviation, analytical and production rate uncertainties).  
536 Radiocarbon ages in cal BP are presented in Jomelli et al. (2017).

537

538 4.3.  $^{36}\text{Cl}$  ages (n=13),  $^{10}\text{Be}$  ages (n=3) and  $^{26}\text{Al}/^{10}\text{Be}$  ratios (n=2) from Arago Glacier site

539

540 At the Arago Glacier sampling site, we dated three moraines, one bedrock surface and three  
541 erratic boulders. The outermost A1 moraine, composed of syenites, was dated using  $^{36}\text{Cl}$  on  
542 feldspar separates from all samples, and  $^{10}\text{Be}$  and  $^{26}\text{Al}$  on quartz of two samples. The bedrock  
543 surface (RDB-13), which was also sampled from a syenite, was dated only with  $^{10}\text{Be}$  and  $^{26}\text{Al}$   
544 on quartz. Finally, the two innermost moraines A2a-b, composed of trachytes and syenites,  
545 were dated with  $^{36}\text{Cl}$  on whole rock and feldspar separates.

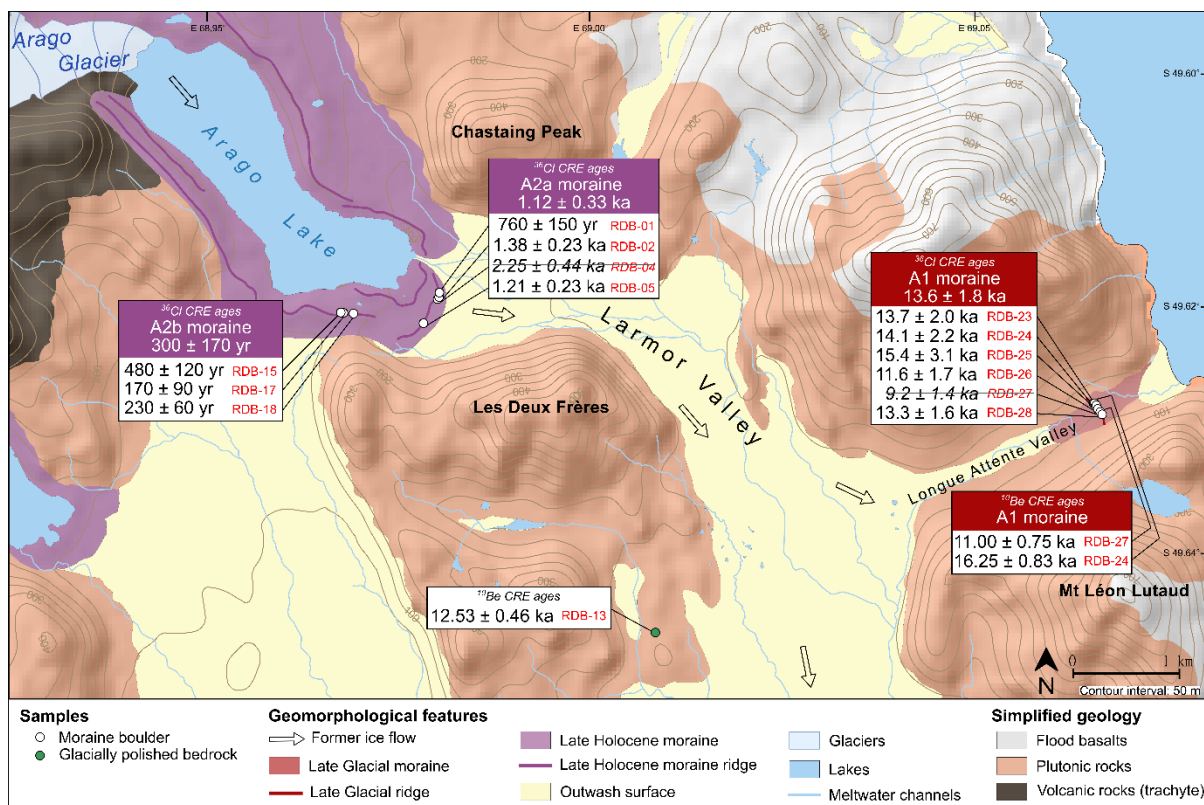
546 The  $^{36}\text{Cl}$  surface exposure ages at the Arago Glacier site range from  $760 \pm 150$  yr to  $15.4 \pm$   
547  $3.1$  ka (Table 4, Fig. 7) and moraine ages are in agreement with their stratigraphic position.  
548 The  $^{36}\text{Cl}$  ages RDB-01, -02, -04 and -05 of the outermost (oldest) A2a moraine are  $760 \pm 150$   
549 yr,  $1.38 \pm 0.23$  ka,  $2.25 \pm 0.44$  ka and  $1.21 \pm 0.23$  ka, respectively. RDB-04 is probably  
550 affected by nuclide inheritance and is rejected as an outlier. The arithmetic mean of the  
551 remaining ages of A2a moraine and total uncertainty are  $1.12 \pm 0.33$  ka (n = 3). On the  
552 innermost (youngest) A2b moraine, samples RDB-15, -17 and -18 give  $^{36}\text{Cl}$  ages of  $480 \pm$   
553  $120$ ,  $170 \pm 90$ ,  $230 \pm 60$  yr and the moraine has a mean age of  $300 \pm 170$  yr.

554 Near Les Deux Frères (in between A1 moraine and A2a-b moraine complex; Fig. 7), the  
555 bedrock sample RDB-13, collected in syenites upstream of A1 moraine, yields a  $^{10}\text{Be}$  age of  
556  $12.53 \pm 0.46$  ka and a  $^{26}\text{Al}/^{10}\text{Be}$  ratio of  $6.48 \pm 0.64$  (Table 5), which is consistent with the

557  $^{26}\text{Al}/^{10}\text{Be}$  production ratio of 6.75 calculated by Balco and Rovey (2008) and Balco et al.  
558 (2008). This age suggests that this bedrock sample has been continuously exposed at the  
559 surface and does not contain any isotopic inheritance from the last interglacial stadial.

560 Samples RDB-23, -24, -25, -26, -27 and -28, which were collected on the top of the  
561 outermost (oldest) A1 moraine have individual ages of  $13.7 \pm 2.0$  ka,  $14.1 \pm 2.2$  ka,  $15.4 \pm$   
562  $3.1$  ka,  $11.6 \pm 1.7$  ka,  $9.2 \pm 1.4$  ka and  $13.3 \pm 1.6$  ka, respectively. RDB-24 and -27 yield  $^{10}\text{Be}$   
563 ages of  $16.25 \pm 0.83$  and  $11.00 \pm 0.75$  ka, respectively (Table 5, Fig. 7). No statistical  
564 difference can be observed between  $^{10}\text{Be}$  CRE ages and  $^{36}\text{Cl}$  CRE ages of these two samples  
565 (Tables 4 and 5). The  $^{10}\text{Be}$  and  $^{36}\text{Cl}$  CRE ages of sample RDB-27 are both the lowest in the  
566 whole age population and have to be related to the high RDB-27  $^{26}\text{Al}/^{10}\text{Be}$  ratio of  $9.42 \pm$   
567  $1.41$  that may indicate that this surface might have been exposed at depth and then re-expose  
568 at surface when recently exhumed (Akçar et al., 2017). Therefore, both  $^{10}\text{Be}$  and  $^{36}\text{Cl}$  CRE  
569 ages are considered as outliers. The  $^{26}\text{Al}$  measurement of RDB-24 did not yield a meaningful  
570 result probably due to analytical issues and is therefore not considered further. The mean  $^{36}\text{Cl}$   
571 age for the A1 moraine, excluding RDB-27, is  $13.6 \pm 1.8$  ka ( $n = 5$ ).

572



573  
574 **Figure 7.** Glacial geomorphological map of the Arago Glacier site. White boxes show  $^{36}\text{Cl}$   
575 and  $^{10}\text{Be}$  sample ages of moraine boulders and bedrock with their inferred analytical  
576 uncertainties. Samples written in *striked-through italic text* are rejected as outliers and  
577 therefore excluded from the discussion. The arithmetic means for moraine groups are shown  
578 in colored boxes with their total uncertainties (i.e. standard deviation, analytical and  
579 production rate uncertainties).

580

581

582

583

584

585

586

587

## 588 5. Discussion

589

### 590 5.1. Timing of glacier fluctuations at Kerguelen Archipelago since the Late Glacial

591 Spanning from ~17,000 to ~70 years, this new surface exposure dataset improves our  
592 knowledge on the Kerguelen glacier fluctuations during the Late Glacial period and the  
593 Holocene (Figs. 4, 6 and 7).

594 <sup>36</sup>Cl dating of a bedrock sample (VLT-04) at an altitude of 437 m a.s.l. at the Val Travers site,  
595 suggests that this location became ice free at  $17.3 \pm 2.2$  ka ago (Fig. 4). This finding is  
596 consistent with previous ages from erratics at the Presqu'île de la Grye (mean age of  $19.8 \pm$   
597  $2.2$  ka) located about 10 km east of Val Travers but at an altitude of about 70 m a.s.l. (Jomelli  
598 et al., 2017). These results indicate that during the beginning of the Late Glacial period a  
599 general deglaciation was occurring (at least in this sector east of CIC).

600 At the bottom of the adjacent valley, a branch of Explorateur glacier deposited the V1  
601 moraine at  $16.0 \pm 1.9$  ka ago, likely during the Heinrich Stadial 1 (HS1; 17.5–14.7 ka;  
602 Rasmussen et al., 2014). However, considering the high uncertainty from this V1 mean  
603 moraine age (1.9 ka), it cannot be excluded that this moraine was instead deposited during the  
604 beginning of the ACR. In any case, this new data provides another evidence of main glacier  
605 extent during this period on the archipelago, as the Belvedere moraine has already been dated  
606 to the HS1/ACR period ( $15.5 \pm 1.8$  ka) on the southwest of the archipelago (Jomelli et al.,  
607 2018). Upstream in Val Travers another moraine deposition (moraine V2) occurred at  $12.9 \pm$   
608  $1.7$  ka ago. Within the calculated uncertainties, this moraine age is consistent with previous  
609 observations near Presqu'île de la Grye, where the Bontemps moraine was formed northeast  
610 of the Val Travers site  $13.6 \pm 1.5$  ka ago by the advance of the Explorateur Glacier (Jomelli et

611 al., 2018; 2017). On Rallier du Baty Peninsula, the A1 moraine of Arago Glacier may have  
612 been formed during the same period at  $13.6 \pm 1.8$  ka ago. Another small debris-covered  
613 glacier (Gentil Glacier) located south of the archipelago on the Gallieni Peninsula, also  
614 experienced glacial advances that occurred at  $14.3 \pm 2.3$  ka (Charton et al., 2020). All these  
615 earlier dated moraines are indistinguishable within the calculated range of uncertainties with  
616 the new age of V2 moraines at Val Travers and the A1 moraine at Rallier du Baty peninsula.  
617 Altogether, these data suggest that during the phase of deglaciation that had started earlier  
618 than about 20 ka, glaciers of the archipelago stagnated or readvanced at least once.

619 Interestingly, no evidence of Early nor Mid-Holocene glacier extents has been found so far,  
620 suggesting that glaciers were smaller at Kerguelen during these periods than they were during  
621 the Late Holocene re-advances (Frenot et al., 1997; Jomelli et al., 2017; Charton et al., 2020).  
622 These Late-Holocene re-advances are corroborated by new evidence at two sites. One such  
623 site is the proglacial margin of Arago Glacier (Fig. 7), where the A2a moraine is dated to the  
624 last millennium ( $1.12 \pm 0.33$  ka ago). Several moraine ridges upstream of A2a moraine,  
625 including the A2b moraine, that was deposited  $300 \pm 170$  yr ago, attest to further glacier  
626 advances or stillstands within the last millennium. Given the absence of moraines between  
627 A1 (Late Glacial) and A2a moraines, it is assumed that the glacier generally receded to at  
628 least this location between the end of the Late Glacial period and the Late Holocene advance.  
629 In addition, the bedrock sample (RDB-13) located on the proglacial margin of the Arago  
630 Glacier in between A1 and A2a-b moraines is dated at  $12.53 \pm 0.46$  ka ago, which suggests  
631 that this area has been ice free since at least 13 ka.

632 In Ampere Glacier's forefield, the oldest Holocene advance is recorded by the outermost M1  
633 moraine and, after Bayesian filtering, is now dated at  $1000 \pm 470$  yr ago ( $1110 \pm 470$  CE). A  
634 subsequent advance led to the formation of the M2 moraine, which is now dated at  $480 \pm 290$



635 yr ago ( $1590 \pm 290$  CE) (Fig. 6). These findings are complemented by  $^{36}\text{Cl}$  dating of erratic  
636 boulders perched on glacially-polished bedrock surfaces on the right-lateral proglacial margin  
637 of the Ampere Glacier located  $\sim 2\text{-}4$  km upstream and  $\sim 90\text{-}250$  m higher than the M2  
638 moraine. The erratic boulder samples yield a mean age of  $\sim 610$  yr (Fig. 6), which is  
639 indistinguishable from the mean ages of M1 and M2. The prolongation of these aligned  
640 boulders can geometrically be connected with the moraine sequence that M1 and M2 are part  
641 of (Fig. 6). Therefore, it is very likely that they represent the former ice margin that can be  
642 related with the formation of one or several of these last-millennium-moraines. Five of the  
643 erratic boulders are paired with glacially-polished bedrock surface samples, with the goal to  
644 constrain the timing of deglaciation and detect potential periods of successive exposure and  
645 burial, indicated by nuclide inheritance in the bedrock surfaces (e.g. Fabel et al., 2002). The  
646 bedrock surfaces at this location were apparently exposed for durations that range between  
647  $\sim 14$  ka and  $\sim 4$  ka. The apparent  $^{36}\text{Cl}$  CRE ages of the bedrock being systematically older than  
648 those of the erratic boulders (mean age  $\sim 610$  yr), confirm a complex history of bedrock  
649 exposure, meaning that the surfaces contain nuclide inheritance from one or several periods  
650 of exposure that pre-date the last-millennium-advances. Given that the apparent bedrock  
651 exposure durations do not exceed  $\sim 14$  ka and that evidence elsewhere from the Kerguelen  
652 Islands shows large glacier extents still at  $\sim 14$  ka and before, we hypothesize the following  
653 exposure-burial scenario. Substantial ice cover during the last glacial cycle eroded these  
654 locations deeply enough to remove any cosmogenic nuclide inventories that might have  
655 accumulated during previous warm periods; following the retreat from the last large glacier  
656 extents of the ACR (at  $\sim 14$  ka), the sample locations experienced deglaciation and  $^{36}\text{Cl}$   
657 started to accumulate continuously until 1 ka. At this stage, the Ampere Glacier re-advanced  
658 and covered these locations again until (latest)  $\sim 150$  yr ago, as approximately suggested by  
659 the nearby moraine sequence and the erratic boulders located on these bedrock surfaces.

660 During this last-millennium-ice-cover, the glacier eroded the subglacial bedrock surfaces and  
661 thus reduced the  $^{36}\text{Cl}$  inventory accumulated between ~14 ka and 1 ka. Varying erosion rates  
662 as a function of topography and related ice velocity led to variable nuclide reduction at the  
663 five bedrock surface locations, thus explaining the range of apparent bedrock exposure  
664 durations. Following this scenario, a first-order estimate indicates that a uniform subglacial  
665 erosion (=abrasion) rate of ~1 mm/yr (corresponding to an abrasion depth of ~85 cm during  
666 the ~850 yr of ice cover) can explain the apparent exposure duration of the sample with the  
667 lowest  $^{36}\text{Cl}$  inventory (MO-09; ~4.4 ka), whereas sample MO-05 (~14.0 ka) would not have  
668 been eroded. Besides abrasion, deep plucking of bedrock is a common subglacial erosion  
669 process that can explain variable Holocene cosmogenic nuclide inventories in nearby bedrock  
670 surfaces (Rand and Goehring, 2019). Holocene subglacial erosion rates between 0.02 and  
671 >1.8 mm/yr have been inferred in crystalline forefields of Alpine glaciers, based on  
672 cosmogenic multi-nuclide methods (Goehring et al., 2011; Schimmelpfennig et al., 2022).  
673 Rates of between 0 and ~1 mm/yr in volcanic (less hard) rocks and the warm-based glacier  
674 setting in Kerguelen seem realistic to explain the apparent variable bedrock exposure  
675 durations and the proposed exposure-burial scenario. We consider the possibility of  
676 significant  $^{36}\text{Cl}$  inventories inherited from earlier warm periods at these locations unlikely, as  
677 no evidence of such warm periods during the last glacial cycle has been provided so far. In  
678 addition, significant discrepancies between paired exposure ages of erratics and glacially-  
679 polished bedrock elsewhere on Kerguelen may also be expected if nuclide inheritance is a  
680 general concern in this setting, like in cold-based glacier sites (Nichols et al., 2019).  
681 However, other existing  $^{36}\text{Cl}$  dates of glacially-polished bedrock on the islands are in good  
682 agreement with nearby erratics and/or the general deglaciation trend for this region since MIS  
683 3 (Jomelli et al., 2017, 2018). This scenario thus suggests that the new bedrock surfaces  
684 investigated in this study were ice-free for most of the Holocene period and provide new

685 evidence that the Kerguelen glaciers had a little extent during most of the Early and Mid-  
686 Holocene.

687

## 688 5.2. Comparison with other paleoglacial records within the southern mid-latitude region

689 The updated  $^{36}\text{Cl}$  dataset consolidates earlier data regarding the Kerguelen glacier  
690 chronologies since the Late Glacial, and it also provides new chronological evidence that the  
691 Kerguelen glacier behavior followed a different Holocene pattern compared to other regions  
692 in the southern mid-latitudes.

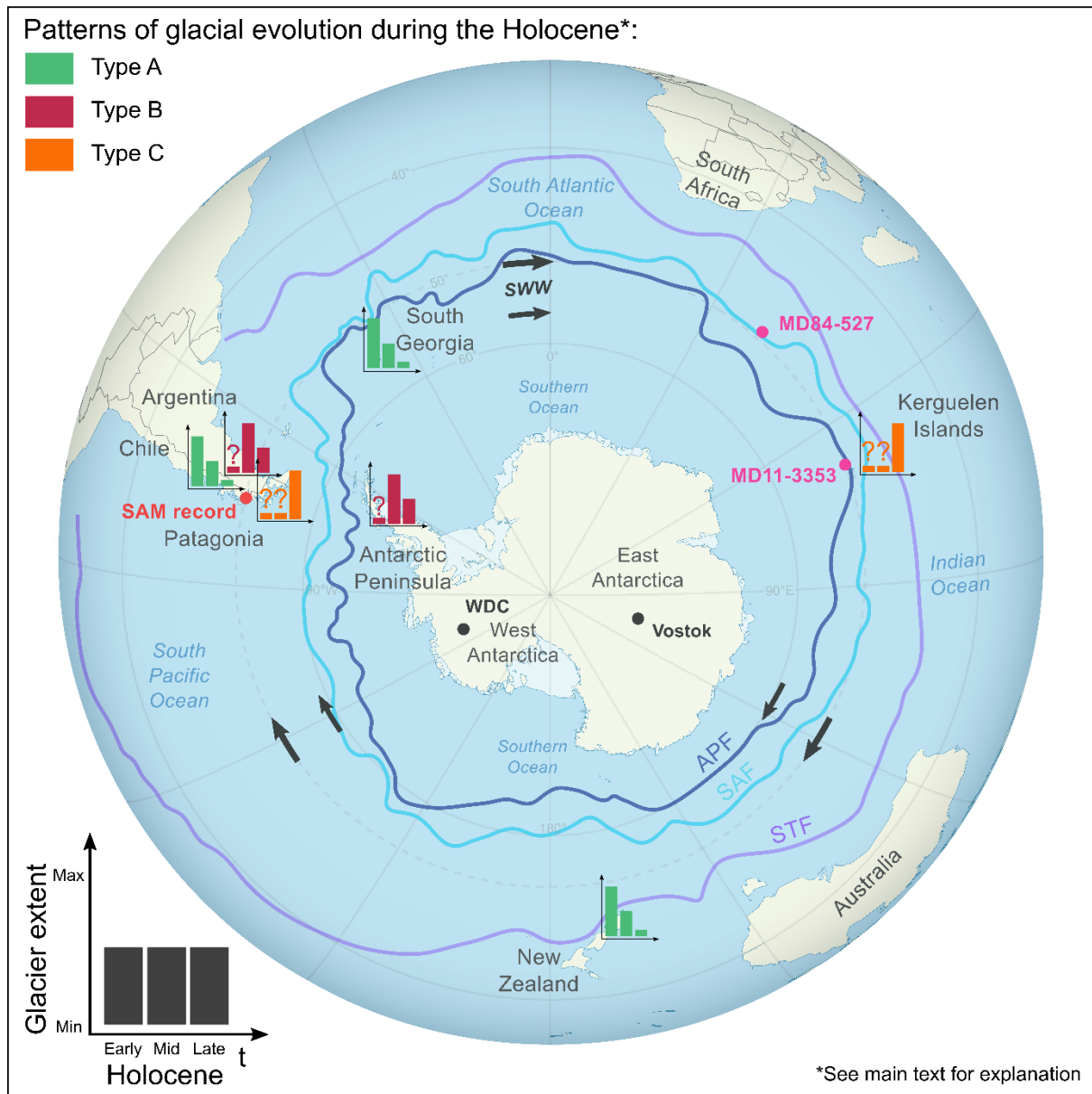
693 Our dataset suggests a possible glacier advance (or stillstand long enough to create a  
694 moraine) during HS1 like in Rakaia valley in New Zealand, where glaciers experienced a  
695 stillstand at ~16 ka in their global recession trend (Putnam et al., 2013). This is at odds with  
696 observations from other southern mid-latitude regions where a global recession of glaciers is  
697 generally recorded (e.g. Hall et al., 2013). Our dataset also indicates a glacier advance during  
698 the ACR, in agreement with findings from other southern mid-latitude regions (e.g. Putnam et  
699 al., 2010a; Pedro et al., 2015; Darvill et al., 2016; Graham et al., 2017). Regarding the  
700 Holocene, we performed a review of published moraine CRE ages of glaciers located in  
701 Patagonia, New Zealand, Antarctic Peninsula and South Georgia, using the alpine ICE-D  
702 database (Balco, 2020) (Fig. 8). Detailed information is available in supplemental material  
703 Table 2, 3 and 4. Based on this evaluation, we identified the following three different patterns  
704 of glacial evolution in this region of the southern mid-latitudes during the Holocene period  
705 (Fig. 8):

706 (i) The first pattern, named type-A (glacier sites n=5), corresponds to a  
707 decreasing glacial extent throughout the Holocene, evidenced by several

708 Early, Mid-and Late Holocene moraines dated in numerous glacial valleys.  
709 Consequently, glaciers experienced their maximum Holocene advance at  
710 the beginning of this period, and then progressively retreated until present-  
711 day. Glaciers following the A-type evolution are located in New-Zealand  
712 (Putnam et al., 2012), north of 50°S in Patagonia (Reynhout et al., 2019),  
713 and South Georgia (Bakke et al., 2021).

714 (ii) The second pattern, type-B (glacier sites n=5), corresponds to small glacial  
715 extents during the Early Holocene, glacier re-advances during the Mid-  
716 Holocene and glacier recession during the Late Holocene. These moraines  
717 exhibit progressively smaller glacier extents, which are dated to the Mid-  
718 and Late Holocene only, and provide evidence of severe glacier retreat  
719 during the Early Holocene. Glaciers following this trend are located in  
720 Patagonia between ~50°S and 55°S (Kaplan et al., 2016) and in the  
721 Antarctic Peninsula (Kaplan et al., 2020 and references therein).

722 (iii) The last pattern, type-C (glacier sites n=4), is mainly based on what has been  
723 documented so far at Kerguelen. According to the currently available  
724 estimates, glaciers were smaller throughout the Early to Mid-Holocene  
725 than during their maximum Late Holocene extent. Hitherto, the only other  
726 location in the Southern Hemisphere where this atypical pattern has been  
727 suggested is in southernmost Patagonia (>55°S) (Reynhout et al., 2021 and  
728 references therein).



729

730 **Figure 8.** Different qualitative patterns of glacial evolution within the southern mid-latitudes  
 731 during the Holocene. Legend information is explained in sections 3.4 and 5.2. The x-axis bar  
 732 of the histograms represents the subperiods of the Holocene (Early Holocene, Mid-Holocene  
 733 and Late Holocene), whereas the y-axis bar represents the qualitative appreciation of glacier  
 734 length (see section 3.4). The question marks above the histogram bars represent missing  
 735 moraines belonging to the referred period in the glacial valley. The black arrow shows the  
 736 modern position of the Southern Westerly Winds (SWW,  $\square$ 50-60°S), the dark blue line  
 737 provides a representation of the modern Antarctic Polar Front (APF), the light blue line is the

738 sub-Antarctic Front (SAF) and the purple line is the sub-Tropical Front (STF). Also shown in  
739 pink dots are the positions of the marine cores, black dots depict the locations of the ice cores  
740 and the single red dot provides the location of the Southern Annular Mode record discussed  
741 in section 5.3.

### 742 5.3. Assessing potential climate drivers of glacier oscillations in Kerguelen Archipelago 743 during the Late Glacial and Holocene

744 The patterns discussed in section 5.2. provide three regionally contrasting Holocene glacier  
745 evolutions within the southern mid-latitude region suggesting complex glacier climatic  
746 relationships at a regional scale in the southern mid-latitudes that need to be further explored.  
747 Here, we do not address the underlying potential climatic puzzle within the whole southern  
748 mid-latitude region but focus on climatic conditions that may have driven glacier fluctuations  
749 at Kerguelen (Fig. 9).

750 We suspect paleoglacier variations at Kerguelen to be strongly impacted by the combined  
751 influence of sea surface temperatures (SSTs) variations and precipitation changes related to  
752 the position of the westerlies, which is partly driven by the SAM. Since air and sea surface  
753 temperatures are significantly correlated at Kerguelen (Favier et al., 2016), paleo SSTs data  
754 around Kerguelen should be more relevant for local temperatures, than remote Antarctic ice  
755 core records. Moreover, reconstructed SSTs combined with subsurface temperatures from the  
756 core MD11-3353 (Fig. 9d and e) located southwest of Kerguelen make it also possible to  
757 document latitudinal changes in the position of the oceanic fronts (Civel-Mazens et al., 2021).

758 As variations of the SAM and the latitudinal gradient of SSTs are not necessarily in phase  
759 through time, they may have acted or not in the same direction on paleoglacier behavior. The  
760 impacts of negative phases of the SAM (SAM-) (more precipitation) and cold SSTs would

761 favor a positive mass balance while the effects of a SAM- and warm SSTs would partly  
762 compensate for each other.

763 Below, we explore links between these two climate drivers and glacier patterns throughout  
764 the Late Glacial and Holocene. Forcings controlling glacier behavior on Kerguelen remain  
765 particularly puzzling for the Late Glacial as precipitation changes and the SAM index for this  
766 period remain unknown. Our dataset reveals a general deglaciation trend interrupted by at  
767 least one glacier advance or stillstand either during HS1 and/or during the ACR. Assuming an  
768 advance or a stillstand during HS1, it would have occurred concomitantly with cold, but  
769 warming, atmospheric conditions recorded in Antarctica (Petit et al., 1999; WAIS Divide  
770 Project Members, 2013; Fig. 9a and b). If occurring during the ACR, it would have been  
771 concordant with the cooling recorded from the Antarctic ice cores (Petit et al., 1999; WAIS  
772 Divide Project Members, 2013; Fig. 9a and b) and elsewhere in the Southern Ocean (Pedro et  
773 al., 2015). We note that warm SSTs seemingly prevailed at that time, as indicated by core  
774 MD11-3353 (Fig. 9d), suggesting that the APF and the SAF were already, and remained, at a  
775 more southern latitude. However, the SST record presents very low resolution over the  
776 deglaciation, and other SST records suggest the ACR was regionally expressed (Labracherie  
777 et al., 1989; Ai et al., 2020; Orme et al., 2020; Civel et al., 2021). The subsurface temperature  
778 record in core MD11-3353 conversely shows a plateau during the ACR in agreement with air  
779 temperature evolution and glacier standstill. During the ACR, increased moisture input has  
780 been reported at the Kerguelen Archipelago, based on multi-proxy analyses of peat sequences  
781 (van der Putten et al., 2015). This might be due to a potential northward shift of the SWW  
782 during this period and might explain a positive glacier mass balance due to enhanced  
783 precipitation. This concept is supported by intensified wet conditions documented from  
784 different proxy records in Patagonia (Davies et al., 2020) suggesting that the SWW were

785 centered at  $\sim 50^{\circ}\text{S}$  during the ACR, while the modern SWW belt lies between  $50^{\circ}\text{S}$  and  $60^{\circ}\text{S}$   
786 (Garreaud et al., 2009).

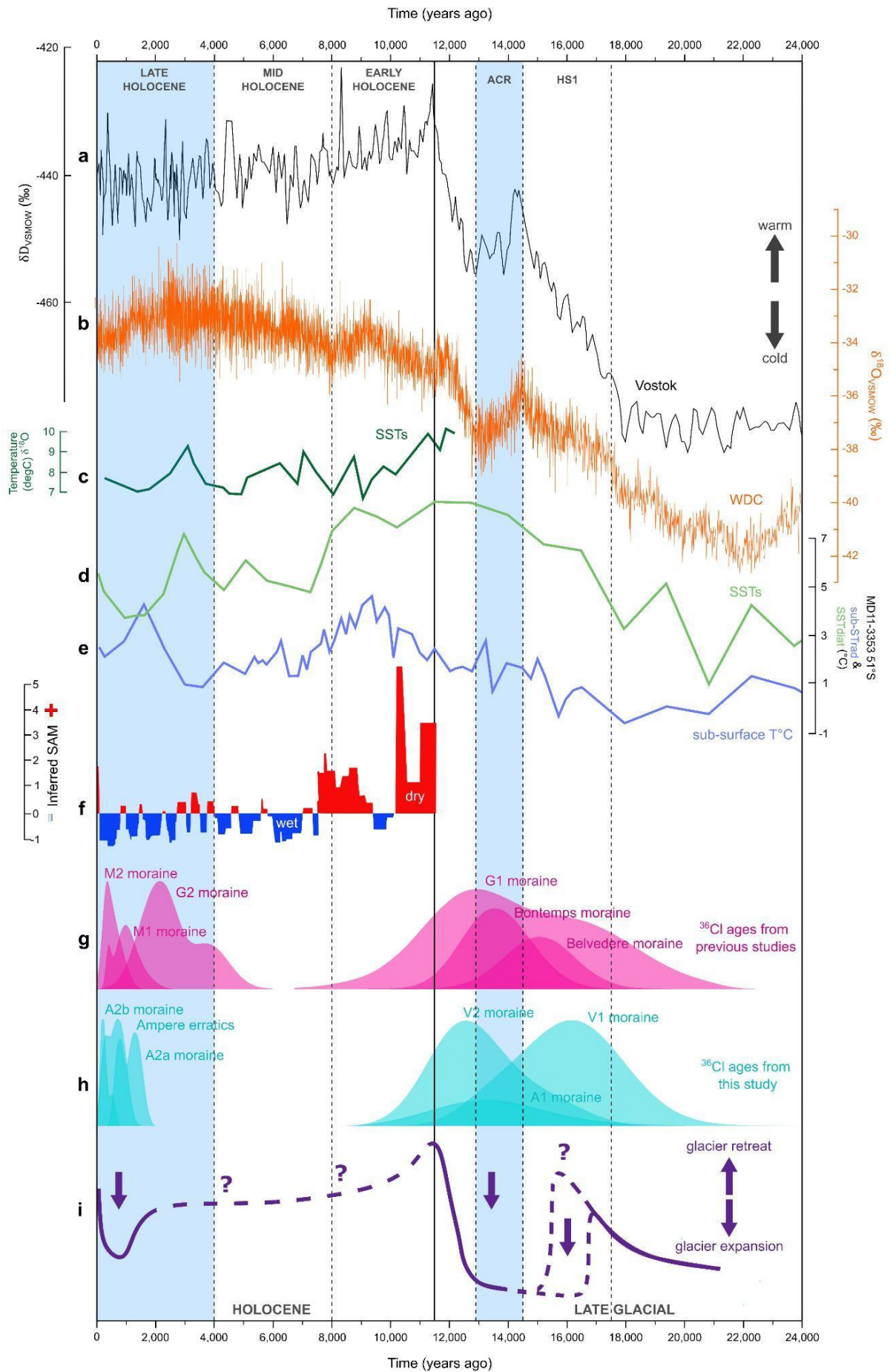
787 During the Holocene a reconstruction of precipitation changes attributed to SAM variations  
788 offers a good opportunity to analyze the influence of the centennial-to-millennial expression  
789 of this climate mode on glacier dynamics at Kerguelen. So far, only one precipitation-SAM  
790 reconstruction spanning the Early to Late Holocene exists, and is inferred from the Lago  
791 Cipreses non-arboreal pollen (NAP) record in Patagonia ( $51^{\circ}\text{S}$ ) (Moreno et al. 2018; Fig. 9f).  
792 According to this record, SAM is mostly characterized by positive-state-like SAM conditions  
793 (less precipitation at the latitude of Kerguelen) during the Early Holocene, i.e. from  $\sim 11.5$  to  
794  $\sim 10.2$  ka, and during the so called ‘Early Warm Dry Anomaly’, from  $\sim 9.5$  to 7.5 ka, which  
795 is in agreement with warm and dry climate conditions from the Kerguelen Islands inferred  
796 from a multi-proxy analyses on a peat record (reconstruction of wind strength, humidity and  
797 relative temperature) investigated by van der Putten et al. (2015). In addition, the Holocene  
798 trend of reconstructed SSTs (Kauffman et al., 2020) near Kerguelen in the Southern Indian  
799 Ocean (shown in Fig. 9c) and southwest of Kerguelen (Civel-Mazens et al., 2021; shown in  
800 Fig. 9d) reveals warmer SSTs during the Early Holocene. Altogether dry conditions, in  
801 response to pervasive SAM+ like conditions, and rather warm SSTs in the region would  
802 explain the relatively small glacier extents at the Kerguelen Archipelago during the Early  
803 Holocene.

804 We notice a cold excursion of SSTs in the Mid-Holocene. Moraines from that time have not  
805 yet been identified. Yet, glaciers might have advanced during the Mid-Holocene, but their  
806 moraines may have been obliterated by the more extensive Late Holocene glacier advances.  
807 However, this potential Mid-Holocene advance may not have lasted long because of the



808 multi-millennial ages of the sampled glacially-polished bedrock, which indicate extensive  
809 deglaciation.

810 During the Late Holocene, negative-state-like SAM conditions increased (Fig. 9f), suggesting  
811 enhanced precipitation, which, combined with rather cold SSTs in the region (Fig. 9c-e),  
812 would have favored glacier re-advance on the Kerguelen Archipelago.



814 **Figure 9.** Comparison of Kerguelen paleoglacier records with Antarctic and southern mid-  
815 latitude climatic proxies (locations are shown in Fig. 8). Proxies for atmospheric temperature  
816 fluctuations are **a.**  $\delta D_{VSMOW}$  (black curve) from Vostok (East Antarctica; Petit et al., 1999)  
817 and **b.**  $\delta^{18}O_{VSMOW}$  (orange curve) from West Antarctica (WAIS Divide Project Members,  
818 2013). **c.** is the SST reconstruction from  $\delta^{18}O$  on planktonic foraminifera (green curve) from  
819 MD84-527 marine core, compiled by Kauffman et al. (2020) but first published by Pichon et  
820 al. (1992). **d.** is the reconstructed subsurface temperatures and **e.** the SSTs, both from the  
821 MD11-3353 core (51°S; Civel-Mazens et al., 2021). **f.** is the Inferred SAM-like index  
822 reconstruction for the Holocene period as shaded boxes (red = positive and blue = negative)  
823 from Lago Cipreses non-arboreal pollen in Patagonia (Moreno et al., 2018). Also shown are  
824 the  $^{36}Cl$  CRE age probability density distributions with their analytical uncertainties only  
825 during the Late Glacial and the Holocene periods from Kerguelen of **g.** previous studies  
826 (Jomelli et al., 2017, 2018; Charton et al., 2020; Verfaillie et al., 2021) and **h.** this study.  
827 Finally, **i.** is a schematic evolution of Kerguelen glacier extents.

828

## 829 6. Conclusion

830 This study aimed to better constrain the evolution of glaciers on the Kerguelen Archipelago,  
831 using *in situ*-produced  $^{36}Cl$  CRE dating from moraine boulders, erratic and glacially-polished  
832 bedrock collected on forefields of the Arago Glacier, Ampere Glacier and in the Val Travers  
833 Valley. Evidence of a Late Glacial glacier advance at the Val Travers site at ~ 16 ka and ~  
834 12.9 ka and at the Arago Glacier at ~ 13.6 is provided, which can likely be related to the HS1  
835 and ACR cold spells. While the finding of the HS1 advance is infrequent, the ACR advance  
836 is consistent with previous results from other locations on the archipelago, and more

837 generally in the southern mid-latitude region, suggesting that glaciers experienced a broadly  
838 synchronous behavior during the ACR.

839 Early and Mid-Holocene glacio-geomorphic features that are testament to glacier advances  
840 have not yet been found on the archipelago. In addition, CRE dating of paired erratic  
841 boulders (~610 yr) and glacially-polished bedrock surfaces (with exposure duration of up to  
842 14 ka) at the Ampere site indicate that this proglacial margin was ice free for several  
843 millennia during the Holocene period. These results, when combined with previously  
844 published radiocarbon-dated peat ages, suggest that the Ampere Glacier was in a retracted  
845 position during most of the Holocene. The new ages also enable refinement of the glacial  
846 chronology for Kerguelen and reveal new Late Holocene advances, at  $\approx 1.12$  ka and  $\approx 300$  yr  
847 at the Arago Glacier site and at  $\sim 1$  ka and  $\sim 430$  yr at the Ampere Glacier site. These findings  
848 suggest that Kerguelen glaciers retreated significantly after their (large) ACR extents and  
849 were smaller than their last-millennium-extents for most of the Holocene. The data also  
850 indicates that the glaciers only re-advanced again from  $\sim 1$  ka. This implies that any moraines  
851 potentially formed during Early and Mid-Holocene were obliterated by the more extensive  
852 Late Holocene glacier extents.

853 To compare this trend with the glacier evolution in other southern mid-latitude regions, a  
854 review of *in situ* cosmogenic data was performed. Three different glacier patterns were  
855 identified within the southern mid-latitudes, implying that glacier/climate relationships across  
856 this region need further investigations. In the Kerguelen region, a rise in nearby SSTs and a  
857 decrease in precipitation, owing to a latitudinal shift of the SWW could explain the relatively  
858 smaller extent of Kerguelen glaciers during the Early Holocene. On the contrary, decreasing  
859 SSTs and increased precipitation during the Mid- and Late Holocene may have led to glacier  
860 expansion in the case of Kerguelen.

861

862 Author contributions

863 VJ, GD, DV, VF, VR, DG and CL conducted the fieldwork on the islands. JC, IS, VJ and GD  
864 participated in producing the cosmogenic data. GA, DB and KK (ASTER Team) performed  
865 accelerator mass spectrometry measurements. JC, IS, VJ, GD, PHB, RB, LM interpreted the  
866 cosmogenic ages; JC, VJ, IS and PHB prepared the figures. All authors contributed to writing  
867 the paper.

868 Acknowledgments

869 This work has received financial support from the LabEx DynamiTe (ANR-11-LABX-0046)  
870 Les Envahisseurs as part of the 'Investissements d'Avenir' programme. This paper was also  
871 supported by the French INSU LEFE Glacepreker project and by the IPEV Kesaaco 1048  
872 project. The  $^{36}\text{Cl}$ ,  $^{10}\text{Be}$  and  $^{26}\text{Al}$  measurements were performed at the ASTER national  
873 accelerator mass spectrometry facility (CEREGE, Aix-en-Provence) that is supported by the  
874 INSU/CNRS, the ANR through the 'Projets thématiques d'excellence' programme for the  
875 'Equipements d'excellence' ASTER-CEREGE action and IRD. We are very thankful for the  
876 compositional analyses at SARM/CRPG (Nancy, France). We also acknowledge the work of  
877 Fatima Mokadem, Laëtitia Léanni and Valery Guillou, who helped processing data.

878

879

880

881

882

883 References:

884 Ai, X.E., Studer, A.S., Sigman, D.M., Martínez-García, A., Fripiat, F., Thöle, L.M., Michel,  
885 E., Gottschalk, J., Arnold, L., Moretti, S., Schmitt, M., Oleynik, S., Jaccard, S.L., Haug,  
886 G.H., 2020. Southern Ocean upwelling, Earth's obliquity, and glacial-interglacial  
887 atmospheric CO<sub>2</sub> change. *Science*, 370(6522), 1348-1352.  
888 <https://doi.org/10.1126/science.abd2115>.

889 Akçar, N., Ivy-Ochs, S., Alfimov, V., Schlunegger, F., Claude, A., Reber, R., Christl, M.,  
890 Vockenhuber, C., Dehnert, A., Rahn, M., Schluchter, C., 2017. Isochron-burial dating of  
891 glaciofluvial deposits: first results from the Swiss Alps. *Earth Surf. Process. Landforms* 42,  
892 2414–2425.

893 Anjar, J., Akçar, N., Larsen, E.A., Lyså, A., Marrero, S., Mozafari, N., Vockenhuber, C.,  
894 2021. Cosmogenic Exposure Dating (<sup>36</sup>Cl) of Landforms on Jan Mayen, North Atlantic, and  
895 the Effects of Bedrock Formation Age Assumptions on <sup>36</sup>Cl Ages. *Geosciences*, 11, 390.  
896 <https://doi.org/10.3390/geosciences11090390>

897 Ansell, H., 2005. Petrology and geochemistry of the 25 Ma Mt. Marion Dufresne basaltic  
898 section on the Kerguelen Archipelago: constraining the transition from Tholeiitic to Mildly  
899 Alkalic volcanism on a major oceanic island, Master of Science – MSc, University of British  
900 Columbia, Canada. <https://doi.org/10.14288/1.0052331>

901 Arnold, M., Merchel, S., Bourles, D., Braucher, R., Benedetti, L., Finkel, R.C., Aumaître, G.,  
902 Gott dang, A., Klein, M., 2010. The French accelerator mass spectrometry facility ASTER:  
903 improved performance and developments. *Nucl. Instrum. Methods Phys. Res. B: Beam*

904 Interactions with Materials and Atoms, 268, 1954-1959.  
905 <https://doi.org/10.1016/j.nimb.2010.02.107>.

906 Bakke, J., Paasche, Ø., Schaefer, J., Timmermann, A., 2021. Long-term demise of sub-  
907 Antarctic glaciers modulated by the Southern Hemisphere Westerlies. *Sci. Rep.* 11, 8361.  
908 <https://doi.org/10.1038/s41598-021-87317-5>

909 Balco, G., Rovey, C., W., 2008. An isochron method for cosmogenic-nuclide dating of buried  
910 soils and sediments. *Am. J. Sci.*, 308 (10) 1083-1114. <https://doi.org/10.2475/10.2008.02>.

911 Balco, G., Stone, J.O., Lifton, N.A., Dunai, T.J., 2008. A complete and easily accessible  
912 means of calculating surface exposure ages or erosion rates from  $^{10}\text{Be}$  and  $^{26}\text{Al}$   
913 measurements. *Quat. Geochronol.*, 3(3), 174-195.  
914 <https://doi.org/10.1016/j.quageo.2007.12.001>.

915 Balco, G., 2020. Technical note: A prototype transparent-middle-layer data management and  
916 analysis infrastructure for cosmogenic-nuclide exposure dating. *Geochronology Discuss.*, 1–  
917 10. <https://doi.org/10.5194/gchron-2020-6>

918 Berthier, E., Bris, R. le, Mabileau, L., Testut, L., Rémy, F., 2009. Ice wastage on the  
919 Kerguelen Islands (49°S, 69°E) between 1963 and 2006. *J. Geophys. Res. Earth Surf.*, 114,  
920 1–11. <https://doi.org/10.1029/2008JF001192>

921 Blard, P.-H., Braucher, R., Lave, J., Bourles, D., 2013. Cosmogenic  $^{10}\text{Be}$  production rate  
922 calibrated against  $^3\text{He}$  in the high Tropical Andes (3800-4900 m, 20-22°S). *Earth Planet. Sci.*  
923 *Lett.* 382, 140-149. <https://doi.org/10.1016/j.epsl.2013.09.010>.

924 Braucher, R., Guillou, V., Bourles, D., Arnold, M., Aumaître, G., Keddadouche, K., Nottoli,  
925 E., 2015. Preparation of ASTER in-house  $^{10}\text{Be}/^9\text{Be}$  standard solutions. *Nucl. Instrum.*

926 Methods Phys. Res. B: Beam Interactions with Materials and Atoms, 361, 335-340.  
927 <https://doi.org/10.1016/j.nimb.2015.06.012>

928 Charton, J., Jomelli, V., Schimmelpfennig, I., Verfaillie, D., Favier, V., Mokadem, F.,  
929 Gilbert, A., Brun, F., Aumaître, G., Bourlès, D.L., Keddadouche, K., 2020. A debris-covered  
930 glacier at Kerguelen (49°S, 69°E) over the past 15 000 years. *Antarct. Sci.*, 33(1), 103–115.  
931 <https://doi.org/10.1017/S0954102020000541>.

932 Chmeleff, J., von Blanckenburg, F, Kossert, K., Jakob, D., 2010. Determination of the <sup>10</sup>Be  
933 half-life by multicollector ICP-MS and liquid scintillation counting. *Nucl. Instrum. Methods*  
934 *Phys. Res. B: Beam Interactions with Materials and Atoms*, 268(2), 192-199.  
935 <https://doi.org/10.1016/j.nimb.2009.09.012>.

936 Civel-Mazens, M., Crosta, X., Cortese, G., Michel, E., Mazaud, A., Ther, O., Ikehara, M.,  
937 Itaki, T., 2021. Impact of the Agulhas Return Current on the oceanography of the Kerguelen  
938 Plateau region, Southern Ocean, over the last 40 kyrs. *Quat. Sci. Rev.*, 251, 106711.  
939 <https://doi.org/10.1016/j.quascirev.2020.106711>

940 Cooley, D., Naveau, P., Jomelli, V. Rabatel, A., Grancher, D., 2006. A bayesian hierarchical  
941 extreme value model for lichenometry. *Environmetrics*, 17, 555-574.

942 Darvill, C.M., Bentley, M.J., Stokes, C.R., Shulmeister, J., 2016. The timing and cause of  
943 glacial advances in the southern mid-latitudes during the last glacial cycle based on a  
944 synthesis of exposure ages from Patagonia and New Zealand. *Quat. Sci. Rev.*, 149, 200–214.  
945 <https://doi.org/10.1016/j.quascirev.2016.07.024>

946 Davies, B.J., Darvill, C.M., Lovell, H., Bendle, J.M., Dowdeswell, J.A., Fabel, D., García,  
947 J.L., Geiger, A., Glasser, N.F., Gheorghiu, D.M., Harrison, S., Hein, A.S., Kaplan, M.R.,  
948 Martin, J.R.V., Mendelova, M., Palmer, A., Pelto, M., Rodés, Á., Sagredo, E.A., Smedley,



949 R.K., Smellie, J.L., Thorndycraft, V.R., 2020. The evolution of the Patagonian Ice Sheet from  
950 35 ka to the present day (PATICE). *Earth-Sci. Rev.*, 204, 103152.  
951 <https://doi.org/10.1016/j.earscirev.2020.103152>

952 Delunel, R., Bourlès, D.L., van der Beek, P.A., Schlunegger, F., Leya, I., Masarik, J., Paquet,  
953 E., 2014. Snow shielding factors for cosmogenic nuclide dating inferred from long-term  
954 neutron detector monitoring. *Quat. Geochronol.*, 24, 16-26.  
955 <https://doi.org/10.1016/j.quageo.2014.07.003>.

956 Dosso, L., Vidal, P., Cantagrel, J-M., Lameyre, J., Marot, A., Zimine, S., 1979. Kerguelen:  
957 continental fragment or oceanic island: petrology and isotopic geochemistry evidence. *Earth*  
958 *Planet. Sci. Lett.*, 43, 46-60.

959

960 Dunai, T.J., Binnie, S.A., Hein, A.S., Paling, S.M., 2014. The effects of a hydrogen-rich  
961 ground cover on cosmogenic thermal neutrons: Implications for exposure dating. *Quat.*  
962 *Geochronol.*, 22, 183–191. <https://doi.org/10.1016/j.quageo.2013.01.001>

963 Favier, V., Verfaillie, D., Berthier, E., Menegoz, M., Jomelli, V., Kay, J.E., Ducret, L.,  
964 Malbêteau, Y., Brunstein, D., Gallée, H., Park, Y.H., Rinterknecht, V., 2016. Atmospheric  
965 drying as the main driver of dramatic glacier wastage in the southern Indian Ocean. *Sci. Rep.*,  
966 6, 1–12. <https://doi.org/10.1038/srep3239>

967 Fink, D., Vogt, S., Hotchkis, M., 2000. Cross-sections for  $^{36}\text{Cl}$  from Ti at  $E_p = 35\text{-}150$  MeV:  
968 Applications to in-situ exposure dating. *Nucl. Instrum. Methods Phys. Res. B: Beam*  
969 *Interactions with Materials and Atoms*, 172, 861–866. <https://doi.org/10.1016/S0168->  
970 [583X\(00\)00200-7](https://doi.org/10.1016/S0168-583X(00)00200-7).

971 Frenot, Y., Gloaguen, J.C., van de Vijver, B., Beyens, L., 1997. Datation de quelques  
972 sediments tourbeux holocènes et oscillations glaciaires aux îles Kerguelen. *Comptes Rendus*  
973 *l'Academie Sci.* 320, 567–573. [https://doi.org/10.1016/S0764-4469\(97\)84712-9](https://doi.org/10.1016/S0764-4469(97)84712-9)

974 Garreaud, R.D., Vuille, M., Compagnucci, R., Marengo, J., 2009. Present-day south  
975 American climate. *Palaeogeogr. Palaeoclimatol. Palaeoecol.*, 281, 180-195.

976 Giret, A., Weis, D., Grégoire, M., Mattielli, N., Moine, B., Michon, G., Scoates, J., Tourpin,  
977 S., Delpech, G., Gerbe, M.-C., Doucet, S., Ethien, R., Cottin, J.-Y., 2003. L'archipel des  
978 Kerguelen: les plus vieilles îles dans le plus jeune océan. *Géologues*, 15–23.

979 Goehring, B.M., Schaefer, J.M., Schluechter, C., Lifton, N.A., Finkel, R.C., Jull, A.J.T.,  
980 Akçar, N., Alley, R.B., 2011. The Rhone Glacier was smaller than today for most of the  
981 Holocene. *Geology*, 39(7), 679–682. <https://doi.org/10.1130/G32145.1>.

982 Gosse, J.C., Phillips, F.M., 2001. Terrestrial in situ cosmogenic nuclides: theory and  
983 application. *Quat. Sci. Rev.* 20, 14, 1475-1560. [https://doi.org/10.1016/S0277-](https://doi.org/10.1016/S0277-3791(00)00171-2)  
984 [3791\(00\)00171-2](https://doi.org/10.1016/S0277-3791(00)00171-2).

985 Graham, A.G.C., Kuhn, G., Meisel, O., Hillenbrand, C.D., Hodgson, D.A., Ehrmann, W.,  
986 Wacker, L., Wintersteller, P., dos Santos Ferreira, C., Römer, M., White, D., Bohrmann, G.,  
987 2017. Major advance of South Georgia glaciers during the Antarctic Cold Reversal following  
988 extensive sub-Antarctic glaciation. *Nat. Commun.* 8, 1-15.  
989 <https://doi.org/10.1038/ncomms14798>.

990 Hall, B.L., Porter, C.T., Denton, G.H., Lowell, T.V., Bromley, G.R.M., 2013. Extensive  
991 recession of Cordillera Darwin glaciers in southernmost South America during Heinrich  
992 Stadial 1. *Quat. Sci. Rev.*, 62, 49-55. <https://doi.org/10.1016/j.quascirev.2012.11.026>.

993 Hall, B.L., Lowell, T.V., Bromley, G.R.M., Denton, G.H., Putnam, A.E., 2019. Holocene  
994 glacier fluctuations on the northern flank of Cordillera Darwin, southernmost South America.  
995 *Quat. Sci. Rev.* 222, 105904 <https://doi.org/10.1016/j.quascirev.2019.105904>.

996 Ivy-Ochs, S., Synal, H.A., Roth, C., Schaller, M., 2004. Initial results from isotope dilution  
997 for Cl and  $^{36}\text{Cl}$  measurements at the PSI/ETH Zurich AMS facility. *Nucl. Instrum. Methods*  
998 *Phys. Res. B: Beam Interactions with Materials and Atoms*, 223–224, 623–627.  
999 <https://doi.org/10.1016/j.nimb.2004.04.115>.

1000 Jomelli, V., Mokadem, F., Schimmelpfennig, I., Chapron, E., Rinterknecht, V., Favier, V.,  
1001 Verfaillie, D., Brunstein, D., Legentil, C., Michel, E., Swingedouw, D., Jaouen, A., Aumaitre,  
1002 G., Bourlès, D.L., Keddadouche, K., 2017. Sub-Antarctic glacier extensions in the Kerguelen  
1003 region (49°S, Indian Ocean) over the past 24,000 years constrained by  $^{36}\text{Cl}$  moraine dating.  
1004 *Quat. Sci. Rev.* 162, 128–144. <https://doi.org/10.1016/j.quascirev.2017.03.010>

1005 Jomelli, V., Schimmelpfennig, I., Favier, V., Mokadem, F., Landais, A., Rinterknecht, V.,  
1006 Brunstein, D., Verfaillie, D., Legentil, C., Aumaitre, G., Bourlès, D.L., Keddadouche, K.,  
1007 2018. Glacier extent in sub-Antarctic Kerguelen archipelago from MIS 3 period: Evidence  
1008 from  $^{36}\text{Cl}$  dating. *Quat. Sci. Rev.* 183, 110–123.  
1009 <https://doi.org/10.1016/j.quascirev.2018.01.008>

1010 Kaplan, M.R., Strelin, J.A., Schaefer, J.M., Denton, G.H., Finkel, R.C., Schwartz, R.,  
1011 Putnam, A.E., Vandergoes, M.J., Goehring, B.M., Travis, S.G., 2011. In-situ cosmogenic  
1012  $^{10}\text{Be}$  production rate at Lago Argentino, Patagonia: implications for late-glacial climate  
1013 chronology. *Earth Planet Sci. Lett.* 309 (1-2), 21-32. [https://](https://doi.org/10.1016/j.epsl.2011.06.018)  
1014 [doi.org/10.1016/j.epsl.2011.06.018](https://doi.org/10.1016/j.epsl.2011.06.018).

1015 Kaplan, M.R., Schaefer, J.M., Strelin, J.A., Denton, G.H., Anderson, R.F., Vandergoes, M.J.,  
1016 Finkel, R.C., Schwartz, R., Travis, S.G., Garcia, J.L., Martini, M.A., Nielsen, S.H.H., 2016.  
1017 Patagonian and southern South Atlantic view of Holocene climate. *Quat. Sci. Rev.* 141, 112–  
1018 125. <https://doi.org/10.1016/j.quascirev.2016.03.014>

1019 Kaplan, M.R., Strelin, J.A., Schaefer, J.M., Peltier, C., Martini, M.A., Flores, E., Winckler,  
1020 G., Schwartz, R., 2020. Holocene glacier behavior around the northern Antarctic Peninsula  
1021 and possible causes. *Earth Planet. Sci. Lett.* 534, 116077.  
1022 <https://doi.org/10.1016/j.epsl.2020.116077>

1023 Kaufman, D.S., McKay, N.P., Routson, C.C., Erb, M., Davis, B.A.S., Heiri, O., Jaccard, S.,  
1024 Tierney, J.E., Dätwyler, C., Axford, Y., Brussel, T., Cartapanis, O., Chase, B.M., Dawson,  
1025 A., de Vernal, A., Engels, S., Jonkers, L., Marsicek, J., Moffa-Sánchez, P., Morrill, C., Orsi,  
1026 A., Rehfeld, K., Saunders, K., Sommer, P.S., Thomas, E., Tonello, M., Tóth, M., Vachula, R.,  
1027 Andreev, A., Bertrand, S., Biskaborn, B., Bringué, M., Brooks, S., Caniupán, M., Chevalier,  
1028 M., Cwynar, L., Emile-Geay, J., Fegyveresi, J., Feurdean, A., Finsinger, W., Fortin, M.-C.,  
1029 Foster, L., Fox, M., Gajewski, K., Grosjean, M., Hausmann, S., Heinrichs, M., Holmes, N.,  
1030 Ilyashuk, B., Ilyashuk, E., Juggins, S., Khider, D., Koinig, K., Langdon, P., Larocque-Tobler,  
1031 I., Li, J., Lotter, A., Luoto, T., Mackay, A., Magyari, E., Malevich, S., Mark, B., Massaferró,  
1032 J., Montade, V., Nazarova, L., Novenko, E., Pařil, P., Pearson, E., Peros, M., Pienitz, R.,  
1033 Płóciennik, M., Porinchu, D., Potito, A., Rees, A., Reinemann, S., Roberts, S., Rolland, N.,  
1034 Salonen, S., Self, A., Seppä, H., Shala, S., St-Jacques, J.-M., Stenni, B., Syrykh, L., Tarrats,  
1035 P., Taylor, K., van den Bos, V., Velle, G., Wahl, E., Walker, I., Wilmshurst, J., Zhang, E.,  
1036 Zhilich, S., 2020. A global database of Holocene paleotemperature records. *Sci. Data*, 7, 1–  
1037 34. <https://doi.org/10.1038/s41597-020-0445-3>

1038 Korschinek, G., Bergmaier, A., Faestermann, T., Gerstmann, U.C., Knie, K., Rugel, G.,  
1039 Wallner, A., Dillmann, I., Dollinger, G., von Gostomski, C.L., Kossert, K., Maiti, M.,  
1040 Poutivtsev, M., Remmert, A., 2010. A new value for the half-life of  $^{10}\text{Be}$  by Heavy-Ion  
1041 Elastic Recoil Detection and liquid scintillation counting. Nucl. Instrum. Methods Phys. Res.  
1042 B: Beam Interactions with Materials and Atoms, 268(2), 187-191.  
1043 <https://doi.org/10.1016/j.nimb.2009.09.020>.

1044 Labracherie, M., Labeyrie, L.D., Duprat, J., Bard, E., Arnold, M., Pichon, J.-J., Duplessy, J.-  
1045 C., 1989. The Last Deglaciation in the Southern Ocean. Paleocyanogr. Paleoclimatol., 4(6),  
1046 629-638. <https://doi.org/10.1029/PA004i006p00629>.

1047 Marrero, S.M., Phillips, F.M., Caffee, M.W., Gosse, J.C., 2016. CRONUS-Earth cosmogenic  
1048  $^{36}\text{Cl}$  calibration. Quat. Geochronol., 31, 199–219.  
1049 <https://doi.org/10.1016/j.quageo.2015.10.002>.

1050 Martin, L., Blard, P.-H., Balco, G., Lave, J., Delunel, R., Lifton, N., Laurent, V., 2017. The  
1051 CREp program and the ICE-D production rate calibration database: a fully parameterizable  
1052 and updated online tool to compute cosmic-ray exposure ages. Quat. Geochronol., 38 (25-4).  
1053 <https://doi.org/10.1016/j.quageo.2016.11.006>.

1054 Martin, L., Blard, P.-H., Lavé, J., Condom, T., Premaillon, M., Jomelli, V., Brunstein, D.,  
1055 Lupker, M., Charreau, J., Mariotti, V., Tibari, B., ASTER Team, Davy, E., 2018. Lake Tauca  
1056 Highstand (Heinrich Stadial 1) driven by a southward shift of the Bolivian High. Sci. Adv., 4,  
1057 1-10. <https://doi.org/10.1126/sciadv.aar2514>.

1058 Merchel, S., Bremser, W., 2004 First international  $^{26}\text{Al}$  interlaboratory comparison - Part I.  
1059 Nuclear Instruments and Methods in Physics Research, Section B: Beam Interactions with  
1060 Materials and Atoms 223–224, 393–400. <https://doi.org/10.1016/j.nimb.2004.04.076>.

1061 Merchel, S., Arnold, M., Aumaître, G., Benedetti, L., Bourlès, D.L., Braucher, R., Alfimov,  
1062 V., Freeman, S.P.H.T., Steier, P., Wallner, A., 2008. Towards more precise  $^{10}\text{Be}$  and  $^{36}\text{Cl}$   
1063 data from measurements at the 10–14 level: Influence of sample preparation. Nucl. Instrum.  
1064 Methods Phys. Res. B: Beam Interactions with Materials and Atoms, 266(22), 4921-4926.  
1065 <https://doi.org/10.1016/j.nimb.2008.07.031>.

1066 Merchel, S., Bremser, W., Alfimov, V., Arnold, M., Aumaître, G., Benedetti, L., Bourlès,  
1067 D.L., Caffee, M., Fifield, L.K., Finkel, R.C., Freeman, S.P.H.T., Martschini, M., Matsushi,  
1068 Y., Rood, D.H., Sasa, K., Steier, P., Takahashi, T., Tamari, M., Tims, S.G., Tosaki, Y.,  
1069 Wilcken, K.M., Xu, S., 2011. Ultra-trace analysis of  $^{36}\text{Cl}$  by accelerator mass spectrometry:  
1070 An interlaboratory study. Anal. Bioanal. Chem. Res., 400, 3125–3132.  
1071 <https://doi.org/10.1007/s00216-011-4979-2>.

1072 Moreno, P.I., Vilanova, I., Villa-Martínez, R., Dunbar, R.B., Mucciarone, D.A., Kaplan,  
1073 M.R., Garreaud, R.D., Rojas, M., Moy, C.M., de Pol-Holz, R., Lambert, F., 2018. Onset and  
1074 Evolution of Southern Annular Mode-Like Changes at Centennial Timescale. Sci. Rep., 8, 1–  
1075 9. <https://doi.org/10.1038/s41598-018-21836-6>

1076 Muscheler, R., Beer, J., Kubik, P.W., Synal, H.-A., 2005. Geomagnetic field intensity during  
1077 the last 60,000 years based on  $^{10}\text{Be}$  and  $^{36}\text{Cl}$  from the Summit ice cores and  $^{14}\text{C}$ . Quat. Sci.  
1078 Rev., 24, 16–17, 1849-1860, <https://doi.org/10.1016/j.quascirev.2005.01.012>.

1079 Naveau, P., Jomelli, V., Cooley, D., Grancher, D. Rabatel, A., 2007. Modeling uncertainties  
1080 in lichenometry studies with an application: The Tropical Andes (Charquini Glacier in  
1081 Bolivia). Arct. Antarct. Alp. Res., 39, 277-288.

1082 Nichols, K. A., Goehring, B. M., Balco, G., Johnson, J. S., Hein, A. S., and Todd, C., 2019.  
1083 New Last Glacial Maximum ice thickness constraints for the Weddell Sea Embayment,  
1084 Antarctica. *The Cryosphere*, 13, 2935–2951, <https://doi.org/10.5194/tc-13-2935-2019>, 2019.

1085 Nicolaysen, K., Frey, F.A., Hodges, K. v., Weis, D., Giret, A., 2000.  $^{40}\text{Ar}/^{39}\text{Ar}$   
1086 geochronology of flood basalts from the Kerguelen Archipelago, southern Indian Ocean:  
1087 Implications for Cenozoic eruption rates of the Kerguelen plume. *Earth Planet. Sci. Lett.*,  
1088 174, 313–328. [https://doi.org/10.1016/S0012-821X\(99\)00271-X](https://doi.org/10.1016/S0012-821X(99)00271-X)

1089 Orme, L.C., Crosta, X., Miettinen<sup>1</sup>, A., Divine, D.V., Husum, K., Isaksson, E., Wacker, L.,  
1090 Mohan, R., Ther, O., Ikehara, M., 2021. Sea surface temperature in the Indian sector of the  
1091 Southern Ocean over the Late Glacial and Holocene. *Clim. Past*, 16, 1451–1467.  
1092 <https://doi.org/10.5194/cp-16-1451-2020>

1093 Park, Y.-H., Durand, I., Kestenare, E., Rougier, G., Zhou, M., d'Ovidio, F., Cotté, C., Lee,  
1094 J.-H., 2014. Polar Front around the Kerguelen Islands: an up-to-date determination and  
1095 associated circulation of surface/subsurface waters. *J. Geophys. Res.: Oceans*, 119, 6575-  
1096 6592. <https://doi.org/10.1002/2014JC010061>

1097 Parnell, A.C., Buck, C.E., Doan, T.K., 2011. A review of statistical chronology models for  
1098 high-resolution, proxy-based Holocene palaeoenvironmental reconstruction. *Quat. Sci. Rev.*,  
1099 30, 2948e2960. <https://doi.org/10.1016/j.quascirev.2011.07.024>

1100 Pedro, J.B., Bostock, H.C., Bitz, C.M., He, F., Vandergoes, M.J., Steig, E.J., Chase, B.M.,  
1101 Krause, C.E., Rasmussen, S.O., Markle, B.R., Cortese, G., 2015. The spatial extent and  
1102 dynamics of the Antarctic Cold Reversal. *Nat. Geosci.*, 9, 1-6,  
1103 <https://doi.org/10.1038/ngeo2580>.

1104 Petit, J.R., Jouzel, J., Raynaud, D., Barkov, N.I., Barnola, J.M., Basile, I., Bender, M.,  
1105 Chappellaz, J., Davis, M., Delaygue, G., Delmotte, M., Kotiyakov, V.M., Legrand, M.,  
1106 Lipenkov, V.Y., Lorius, C., Pépin, L., Ritz, C., Saltzman, E., Stievenard, M., 1999. Climate  
1107 and atmospheric history of the past 420,000 years from the Vostok ice core, Antarctica.  
1108 *Nature*, 399, 429–436. <https://doi.org/10.1038/20859>

1109 Phillips, F. M., Plummer, M. A., 1996. CHLOE: A program for interpreting in-situ cosmo-  
1110 genic nuclide data for surface exposure dating and erosion studies. Abstracts of the 7th  
1111 international conference on Accelerator mass spectrometry, 98–99.

1112 Phillips, F. M., Stone, W. D., Fabryka-Martin, J. T., 2001. An improved approach to  
1113 calculating low-energy cosmic-ray neutron fluxes near the land/atmosphere interface. *Chem.*  
1114 *Geol.*, 175, 689–701, [https://doi.org/10.1016/S0009-2541\(00\)00329-6](https://doi.org/10.1016/S0009-2541(00)00329-6).

1115 Pichon, J.-J., Labeyrie, L.D., Bareille, G., Labracherie, M., Duprat, J., Jouzel, J., 1992.  
1116 Surface water temperature changes in the high latitudes of the southern hemisphere over the  
1117 last glacial-interglacial cycle. *Paleoceanography*, 7, 289–318.

1118 Ponthus, L., 2018. Origine, évolution et mise en place d'un pluton récent en contexte  
1119 intraplaque océanique. Exemple du complexe sud de Rallier du Baty, Kerguelen (T.A.A.F.),  
1120 Ph.D. thesis, Université Toulouse 3 Paul Sabatier, France.

1121 Ponthus, L., de Saint Blanquat, M., Guillaume, D., Le Romancer, M., Pearson, N., O'Reilly,  
1122 S.Y., Grégoire, M., 2020. Plutonic processes in transitional oceanic plateau crust: structure,  
1123 age and emplacement in the South Rallier du Baty laccolith, Kerguelen Islands. *Terra Nova*,  
1124 32, 408-414.

1125 Putnam, A.E., Denton, G.H., Schaefer, J.M., Barrell, D.J.A., Andersen, B.G., Finkel, R.C.,  
1126 Schwartz, R., Doughty, A.M., Kaplan, M.R., Schlüchter, C., 2010a. Glacier advance in



1127 southern middle-latitudes during the Antarctic Cold Reversal. *Nat. Geosci.*, 3, 700–704.  
1128 <https://doi.org/10.1038/ngeo962>

1129 Putnam, A.E., Schaefer, J.M., Barrell, D.J.A., Vandergoes, M., Denton, G.H., Kaplan, M.R.,  
1130 Finkel, R.C., Schwartz, R., Goehring, B.M., Kelley, S.E., 2010b. In situ cosmogenic  $^{10}\text{Be}$   
1131 production-rate calibration from the Southern Alps, New Zealand. *Quat. Geochronol.* 5 (4),  
1132 392-409. <https://doi.org/10.1016/j.quageo.2009.12.001>.

1133 Putnam, A.E., Schaefer, J.M., Denton, G.H., Barrell, D.J.A., Finkel, R.C., Andersen, B.G.,  
1134 Schwartz, R., Chinn, T.J.H., Doughty, A.M., 2012. Regional climate control of glaciers in  
1135 New Zealand and Europe during the pre-industrial Holocene. *Nat. Geosci.*, 5, 1–4.  
1136 <https://doi.org/10.1038/ngeo1548>

1137 Putnam, A.E., Schaefer, J.M., Denton, G.H., Barrell, D.J.A., Andersen, B.G., Koffman,  
1138 T.N.B., Rowan, A.V., Finkel, R.C., Rood, D.H., Schwartz, R., Vandergoes, M.J., Plummer,  
1139 M.A., Brocklehurst, S.H., Kelley, S.E., Ladig, K.L., 2013. Warming and glacier recession in  
1140 the Rakaia valley, Southern Alps of New Zealand, during Heinrich Stadial 1. *Earth Planet.*  
1141 *Sci. Lett.*, 382, 98-110. <http://doi.org/10.1016/j.epsl.2013.09.005>

1142 Rand, C., Goehring, B., 2019. The distribution and magnitude of subglacial erosion on  
1143 millennial timescales at Engabreen, Norway. *Ann. Glaciol.*, 60(80), 73-81.  
1144 <https://doi.org/10.1017/aog.2019.42>

1145 Rasmussen, S.O., Bigler, M., Blockley, S.P., Blunier, T., Buchardt, S.L., Clausen, H.B.,  
1146 Cvijanovic, I., Dahl-Jensen, D., Johnsen, S.J., Fischer, H., Gkinis, V., Guillevic, M., Hoek,  
1147 W.Z., Lowe, J.J., Pedro, J.B., Popp, T., Seierstad, I.K., Steffensen, J.P., Svensson, A.M.,  
1148 Vallelonga, P., Vinther, B.M., Walker, M.J.C., Wheatley, J.J., Winstrup, M., 2014. A  
1149 stratigraphic framework for abrupt climatic changes during the Last Glacial period based on

1150 three synchronized Greenland ice-core records: refining and extending the INTIMATE event  
1151 stratigraphy, *Quat. Sci. Rev.*, 106, 14-28, <https://doi.org/10.1016/j.quascirev.2014.09.007>.

1152 Raup, B., Racoviteanu, A., Khalsa, S.J.S., Helm, C., Armstrong, R., Arnaud, Y., 2007. The  
1153 GLIMS geospatial glacier database: a new tool for studying glacier change. *Glob. Planet.*  
1154 *Change*, 56. <https://doi.org/10.1016/j.gloplacha.2006.07.018>.

1155 Reynhout, S.A., Sagredo, E.A., Kaplan, M.R., Aravena, J.C., Martini, M.A., Moreno, P.I.,  
1156 Rojas, M., Schwartz, R., Schaefer, J.M., 2019. Holocene glacier fluctuations in Patagonia are  
1157 modulated by summer insolation intensity and paced by Southern Annular Mode-like  
1158 variability. *Quat. Sci. Rev.* 220, 178-187. <https://doi.org/10.1016/j.quascirev.2019.05.029>.

1159 Reynhout, S., Kaplan, M., Sagredo, E., Aravena, J., Soteres, R., Schwartz, R., Schaefer, J.,  
1160 2021. Holocene glacier history of northeastern Cordillera Darwin, southernmost South  
1161 America (55°S). *Quat. Res.*, 105, 1-16. <https://doi.org/10.1017/qua.2021.45>

1162 Rudolph, E.M., Hedding, D.W., Fabel, D., Hodgson, D.A., Gheorghiu, D.M., Shanks, R.,  
1163 Nel, W., 2020. Early glacial maximum and deglaciation at sub-Antarctic Marion Island from  
1164 cosmogenic  $^{36}\text{Cl}$  exposure dating. *Quat. Sci. Rev.*, 231.  
1165 <https://doi.org/10.1016/j.quascirev.2020.106208>

1166 Sarıkaya, M.A., Çiner, A., Zreda, M., Şen, E., Ersoy, O., 2018. Chlorine degassing  
1167 constrained by cosmogenic  $^{36}\text{Cl}$  and radiocarbon dating of early Holocene rhyodacitic lava  
1168 domes on Erciyes stratovolcano, central Turkey. *J. Volcanol. Geotherm. Res.*, 369, 263-275,  
1169 <https://doi.org/10.1016/j.jvolgeores.2018.11.029>.

1170 Schimmelpfennig, I., 2009. Cosmogenic  $^{36}\text{Cl}$  in Ca and K rich minerals: analytical  
1171 developments, production rate calibrations and cross calibration with  $^3\text{He}$  and  $^{21}\text{Ne}$ , Ph.D.  
1172 thesis, Université Paul Cézanne - Aix-Marseille III, France.

1173 Schimmelpfennig, I., Benedetti, L., Finkel, R., Pik, R., Blard, P.H., Bourlès, D., Burnard, P.,  
1174 Williams, A., 2009. Sources of in-situ  $^{36}\text{Cl}$  in basaltic rocks. Implications for calibration of  
1175 production rates. *Quat. Geochronol.*, 4, 441–461.  
1176 <https://doi.org/10.1016/j.quageo.2009.06.003>

1177 Schimmelpfennig, I., Benedetti, L., Garreta, V., Pik, R., Blard, P.H., Burnard, P., Bourlès, D.,  
1178 Finkel, R., Ammon, K., Dunai, T., 2011. Calibration of cosmogenic  $^{36}\text{Cl}$  production rates  
1179 from Ca and K spallation in lava flows from Mt. Etna (38°N, Italy) and Payun Matru (36°S,  
1180 Argentina). *Geochim. Cosmochim. Acta*, 75, 2611–2632.  
1181 <https://doi.org/10.1016/j.gca.2011.02.013>

1182 Schimmelpfennig, I., Schaefer, J.M., Putnam, A.E., Koffman, T., Benedetti, L., Ivy-Ochs, S.,  
1183 Schlüchter, C., Arnold, M., Aumaître, G., Bourlès, D., Keddadouche, K., 2014.  $^{36}\text{Cl}$   
1184 production rate from K-spallation in the European Alps (Chironico landslide, Switzerland). *J.*  
1185 *Quat. Sci.*, 29, 407–413. <https://doi.org/10.1002/jqs.2720>

1186 Schimmelpfennig, I., Schaefer, J., Lamp, J., Godard, V., Schwartz, R., Bard, E., Tuna, T.,  
1187 Akçar, N., Schlüchter, C., Zimmerman, S. R., ASTER Team, 2022. Glacier response to  
1188 Holocene warmth inferred from in situ  $^{10}\text{Be}$  and  $^{14}\text{C}$  bedrock analyses in Steingletscher's  
1189 forefield (central Swiss Alps), *Clim. Past* 18, 23-44. <https://doi.org/10.5194/cp-18-23-2022>

1190 Solomina, O.N., Bradley, R.S., Jomelli, V., Geirsdottir, A., Kaufman, D.S., Koch, J., McKay,  
1191 N.P., Masiokas, M., Miller, G., Nesje, A., Nicolussi, K., Owen, L.A., Putnam, A.E., Wanner,  
1192 H., Wiles, G., Yang, B., 2016. Glacier fluctuations during the past 2000 years. *Quat. Sci.*  
1193 *Rev.*, 149, 61–90. <https://doi.org/10.1016/j.quascirev.2016.04.008>

1194 Sokolov, S., Rintoul, S.R., 2009. Circumpolar structure and distribution of the Ant-  
1195 arctic Circumpolar Current fronts: 2. Variability and relationship to sea surface height. *J. Geophys.*  
1196 *Res.* 114 <https://doi.org/10.1029/2008JC005248>

1197 Stone, J.O., 2000. Isotope production. *J. Geophys. Res.*, 105, 753–759.

1198 Stone, J.O., Fifield, K., Vasconcelos, P., 2005. Terrestrial chlorine-36 production from  
1199 spallation of iron, in: Abstract of 10th International Conference on Accelerator Mass  
1200 Spectrometry.

1201 Taylor, J. R., 1997. An Introduction to Error Analysis. The Study of Uncertainties in Physical  
1202 Measurements. University Science Books, Sausalito, USA.

1203 Thompson, D.W.J., Solomon, S., Kushner, P.J., England, M.H., Grise, K.M., Karoly, D.J.,  
1204 2011. Signatures of the Antarctic ozone hole in Southern Hemisphere surface climate change.  
1205 *Nat. Geosci.*, 4, 741–749. <https://doi.org/10.1038/ngeo1296>

1206 Uppala, S.M., Kållberg, P.W., Simmons, A.J., Andrae, U., Bechtold, V.D.C., Fiorino, M.,  
1207 Gibson, J.K., Haseler, J., Hernandez, A., Kelly, G.A., Li, X., Onogi, K., Saarinen, S., Sokka,  
1208 N., Allan, R.P., Andersson, E., Arpe, K., Balmaseda, M.A., Beljaars, A.C.M., Berg, L.V.D.,  
1209 Bidlot, J., Bormann, N., Caires, S., Chevallier, F., Dethof, A., Dragosavac, M., Fisher, M.,  
1210 Fuentes, M., Hagemann, S., Hólm, E., Hoskins, B.J., Isaksen, I., Janssen, P.A.E.M., Jenne,  
1211 R., McNally, A.P., Mahfouf, J.-F., Morcrette, J.-J., Rayner, N.A., Saunders, R.W., Simon, P.,  
1212 Sterl, A., Trenberth, K.E., Untch, A., Vasiljevic, D., Viterbo, P., Woollen, J., 2005. The  
1213 ERA-40 re-analysis. *Q.J.R. Meteorol. Soc.*, 131, 2961-3012.  
1214 <https://doi.org/10.1256/qj.04.176>.

1215 van der Putten, N., Verbruggen, C., Björck, S., Michel, E., Disnar, J.R., Chapron, E., Moine,  
1216 B.N., de Beaulieu, J.L., 2015. The Last Termination in the South Indian Ocean: A unique

1217 terrestrial record from Kerguelen Islands (49°S) situated within the Southern Hemisphere  
1218 westerly belt. *Quat. Sci. Rev.*, 122, 142–157. <https://doi.org/10.1016/j.quascirev.2015.05.010>

1219 Verfaillie, D., Favier, V., Dumont, M., Jomelli, V., Gilbert, A., Brunstein, D., Gallée, H.,  
1220 Rinterknecht, V., Menegoz, M., Frenot, Y., 2015. Recent glacier decline in the Kerguelen  
1221 Islands (49°S, 69°E) derived from modeling , field observations , and satellite data. *J.*  
1222 *Geophys. Res. Earth Surf.*, 120, 637–654. <https://doi.org/10.1002/2014JF003329>.

1223 Verfaillie, D., Favier, V., Gallée, H., Fettweis, X., Agosta, C., Jomelli, V., 2019. Regional  
1224 modeling of surface mass balance on the Cook Ice Cap, Kerguelen Islands (49°S, 69°E).  
1225 *Clim. Dyn.*, 53, 5909–5925. <https://doi.org/10.1007/s00382-019-04904-z>

1226 Verfaillie, D., Charton, J., Schimmelpfennig, I., Stroebele, Z., Jomelli, V., Bétard, F., Favier,  
1227 V., Cavero, J., Berthier, E., Goosse, H., Rinterknecht, V., Legentil, C., Charrassin, R.,  
1228 Aumaître, G., Boulès, D.L., Keddadouche, K., 2021. Evolution of the Cook Ice Cap  
1229 (Kerguelen Islands) between the last centuries and 2100 CE based on cosmogenic dating and  
1230 glacio-climatic modelling. *Antarct. Sci.*, 33(3), 301-317.  
1231 <https://doi.org/10.1017/S0954102021000080>

1232 WAIS Divide Project Members, 2013. Onset of deglacial warming in West Antarctica driven  
1233 by local orbital forcing. *Nature* 500, 440–444. <https://doi.org/10.1038/nature12376>

1234 Ward, G.K., Wilson, S.R., 1978. Procedures for comparing and combining radiocarbon age  
1235 determinations: A critique. *Archaeometry*, 20, 19–31. [https://doi.org/10.1111/j.1475-](https://doi.org/10.1111/j.1475-4754.1978.tb00208.x)  
1236 [4754.1978.tb00208.x](https://doi.org/10.1111/j.1475-4754.1978.tb00208.x).

1237 Zreda, M.G., Phillips, F.M., Kubik, P.W., Sharma, P., Elmore, D., 1993. Cosmogenic <sup>36</sup>Cl  
1238 dating of young basaltic eruption complex, Lathrop Wells, Nevada. *Geology*, 21, 57–60.

1239 Zweck, C., Zreda, M., Desilets, D., 2013. Snow shielding factors for cosmogenic nuclide  
1240 dating inferred from Monte Carlo neutron transport simulations. *Earth Planet. Sci. Lett.*, 379,  
1241 64-71. <https://doi.org/10.1016/j.epsl.2013.07.023>.